Warming above, cooling below: First model-based quantitative thermal-regime assessment and subsurface thermal evolution of Nivlisen Ice Shelf, East Antarctica, revealing non-equilibrium thermal adjustment and progressive thermal preconditioning

Geetha Priya M*, Deva Jefflin A R, Adithya Sunil

Centre for Incubation, Innovation, Research and Consultancy, Jyothy Institute of Technology, Bengaluru-560082.

*geetha.sri82@gmail.com

Abstract

We present the first quantitative thermal characterisation of Nivlisen Ice Shelf, central Dronning Maud Land, East Antarctica, using a one-dimensional heat-transfer model forced by ERA5 surface skin temperatures (1940–2025). For the primary scenario (H = 312 m), the steady-state solution yields a mid-column temperature of −4.89 °C, Péclet number Pe = 4 (intermediate conduction–advection regime), thermal equilibration timescale τ = 269 yr, basal conductive heat flux of 14.22 mW m^{-2}, and conductive basal melt rate of 1.49 mm yr^{-1}. Seasonal temperature variations penetrate to an e-folding depth of 3.42 m, with the firn layer effectively isolating ice below ~20 m from seasonal forcing. Transient simulations reveal significant surface warming of +0.60 °C $decade^{-1}$ (R^2 = 0.622, $p < 0.0001$). Temperatures increase at +0.57 and +0.31 °C $decade^{-1}$ at 1 m and 10 m depth, respectively, but decrease at −0.23 °C $decade^{-1}$ at 100 m depth (R^2 = 0.995), producing a sign reversal at ~27 m depth. This non-equilibrium structure reflects an equilibration timescale substantially longer than the 86-year forcing record. Near-surface cold content at 1 m depth decreased by 36.1% (38.96 to 24.91 MJ m^{-3}), the melt-energy barrier declined by 38.3% (40.05 to 24.72 MJ m^{-3}), and the temperature deficit to the 0°C melt threshold decreased by 78.8% (2.89 to 0.61 °C). Together, these metrics quantify progressive thermal preconditioning through depletion of the near-surface cold reservoir and melt-energy barrier. Model-class uncertainty assessed using the Fimbulisen S1 borehole analogue yielded a conservative upper-bound uncertainty of ±8.69 °C. The results demonstrate that NIS is undergoing progressive thermal preconditioning while remaining in a state of long-term thermal disequilibrium.

Keywords: Nivlisen Ice Shelf, Thermal regime, Hydrofracture, Heat conduction model, East Antarctica, ERA5.

1. INTRODUCTION

1.1 Ice shelf thermal regime and structural stability

Ice shelves are the floating extensions of the Antarctic Ice Sheet that exert a critical buttressing force on outlet glaciers, modulating their contribution to global sea level rise (Morlighem et al., 2020; Scambos et al., 2000). The thermal state of an ice shelf is a fundamental determinant of its mechanical behaviour. Temperature governs the viscosity and fracture toughness of ice, controls the refreezing capacity of the firn layer, and determines how efficiently meltwater hydraulic loads are transmitted to the ice skeleton (C. J.van der Veen, 2007; K.M. Cuffey, 2010). When surface meltwater accumulates on an ice shelf whose firn layer has been thermally depleted, the absence of a refreezing buffer allows water pressure to

drive fracture propagation, a process known as hydrofracture, which has been implicated in the collapse of Larsen B (2002), Wilkins (2008), and Conger-Glenzer (2022) ice shelves (Banwell et al., 2013; Walker et al., 2024; Scambos et al., 2000).

The thermal regime of an ice shelf is set by the balance between surface temperature forcing, basal ocean temperature, internal conduction, and, where applicable, advection by ice flow. For shelves with low Péclet numbers ($Pe = \rho c_p \times acc \times H / k << 1$), conduction dominates and the 1D (Robin, 1955)equation provides an adequate description of the steady-state temperature profile.The Péclet number for NIS at its mean thickness ($Pe \approx 4$ indicates that conductive heat transport is the primary control while accumulation-driven advection remains non-negligible, supporting the use of a 1D conductive framework as a first-order representation.

1.2 Nivlisen Ice Shelf — a region of documented and accelerating surface melt

Nivlisen Ice Shelf (NIS) is located in central Dronning Maud Land (cDML), East Antarctica, at approximately 70.3°S, 11.3°E, in the vicinity of the Schirmacher Oasis. It hosts two Indian Antarctic stations (Maitri) and is among the better-characterised ice shelves in East Antarctica in terms of its surface mass balance (Pratap et al., 2022) , basal melt distribution (Lindbäck et al., 2019) , and surface hydrology (Geetha Priya et al., 2024; Geetha Priya et al., 2023). Basal melt rates at NIS are moderate overall (~0.8 m yr^{-1}; (Lindbäck et al., 2019), with seasonal variability driven by ocean surface water rather than warm deep-water intrusion, confirming a cold-water cavity thermal regime (Lindbäck et al., 2019).

Surface melt at NIS is well documented. Trusel et al., (2013) estimated surface melt rates of ~80 mm w.e. yr^{-1} from satellite radar backscatter, the second highest in cDML after Roi Baudouin. (Geetha Priya et al., 2023)documented consistent melt pond and supraglacial lake expansion post-2015, with localised events exceeding 1 km^2 in area. Geetha Priya et al., (2023) characterised temporal patterns of surface warming and melting across the shelf. Most critically, Geetha Priya et al., (2026; preprint)applied a linear elastic fracture mechanics (LEFM) framework to ten supraglacial melt ponds observed over 11 austral summers (2015–2026), showing that LEFM-derived stress intensity factors exceeded the reported fracture toughness range of glacier ice at multiple pond locations, with the January 2026 event producing a system-wide network response. These findings establish NIS as a shelf that may have entered conditions consistent with hydrofracture susceptibility, as inferred from LEFM stress intensity factor analysis.

1.3 The knowledge gap — no prior thermal characterisation exists

Despite its documented surface melt activity and growing mechanical vulnerability, no published study has characterised the bulk thermal regime of NIS from numerical modelling or in-situ observations. The absence of a thermal baseline prevents quantitative assessment of the rate at which the firn column is losing its cold storage capacity, the physical process that directly controls firn air content, meltwater refreezing, and the efficiency of hydraulic load transmission. Recent studies have documented increasing surface melt, supraglacial lake expansion, and fracture-mechanical indicators of hydrofracture susceptibility at NIS. However, these studies primarily describe surface manifestations of instability and do not address the thermal state of the firn and ice column that governs cold-content storage, meltwater refreezing potential, and thermal preconditioning. Consequently, a critical process-level gap remains

between observations of surface change and understanding of the subsurface thermal conditions that may facilitate those changes. Recent cold-regions studies have similarly emphasized that subsurface thermal evolution provides critical information on system stability that cannot be inferred from surface observations alone (Alphonse et al., 2026).

This study addresses that gap directly. In doing so it provides the first quantitative thermal baseline for NIS, a reference state against which future thermistor deployments, satellite-derived surface temperature records, and ice–ocean model projections of NIS stability can be benchmarked (Krishna et al., 2026; preprint). The absence of this baseline until now means that the rate of thermal preconditioning at NIS has been entirely unmonitored.

1.4 Surface warming context

ERA5 (European Centre for Medium-Range Weather Forecasts (ECMWF) Reanalysis v5) reanalysis surface skin temperature at NIS centroid shows a statistically significant warming trend of +0.60°C decade^{-1} over 1940–2025. The annual maximum skin temperature trend is +0.117°C decade^{-1} ($p = 0.007$). The Novo AWS records positive degree days (PDDs) of up to 58.9°C·days yr^{-1} (2019), consistent with the documented increase in melt pond formation post-2015. A NASA (National Aeronautics and Space Administration) Landsat 9 image from 6 January 2026 provides visual context for the surface melt environment, showing cerulean-blue meltwater in drainage channels on NIS (https://science.nasa.gov/earth/earth-observatory/seeing-blue-during-schirmachers-summer-melt-season/). These observations, viewed alongside the LEFM results of (Geetha Priya et al., 2026; preprint) , motivate a quantitative characterisation of the thermal state that may contribute to the observed evolution of surface melt and hydrofracture susceptibility at NIS.

1.5 Study objectives

This study has four explicit objectives:

a) To characterise the steady-state thermal structure of NIS across its full observed thickness range, establishing a reference thermal profile for each scenario.
b) To quantify the seasonal and decadal evolution of near-surface and column temperatures from 1940 to 2025 using ERA5-forced transient modelling.
c) To establish a suite of thermal preconditioning metrics that quantify the progressive depletion of the firn thermal buffer and evaluate whether thermal depletion is consistent with the emergence of hydrofracture-susceptible conditions.
d) To provide the first quantitative thermal baseline for NIS for use in future monitoring, modelling, and stability assessment studies.

2. Study Area

The Nivlisen Ice Shelf (NIS) is located along the Princess Astrid Coast of central Dronning Maud Land, East Antarctica, at approximately 70.3°S, 11.3°E (Fig. 1). The shelf occupies an area of ~7,228 km² and is bounded by the Leningradkollen and Djupranen ice rises. BedMachine Antarctica v4 data indicate a mean ice thickness of 311.49 m, with substantial spatial variability across the shelf. NIS experiences moderate surface accumulation and basal melting and is recognized as one of the most melt-sensitive ice shelves in central Dronning Maud Land. Additional details regarding ice-shelf geometry, surface mass balance, basal melting, and surface melt characteristics are provided in Supplementary Section S1.

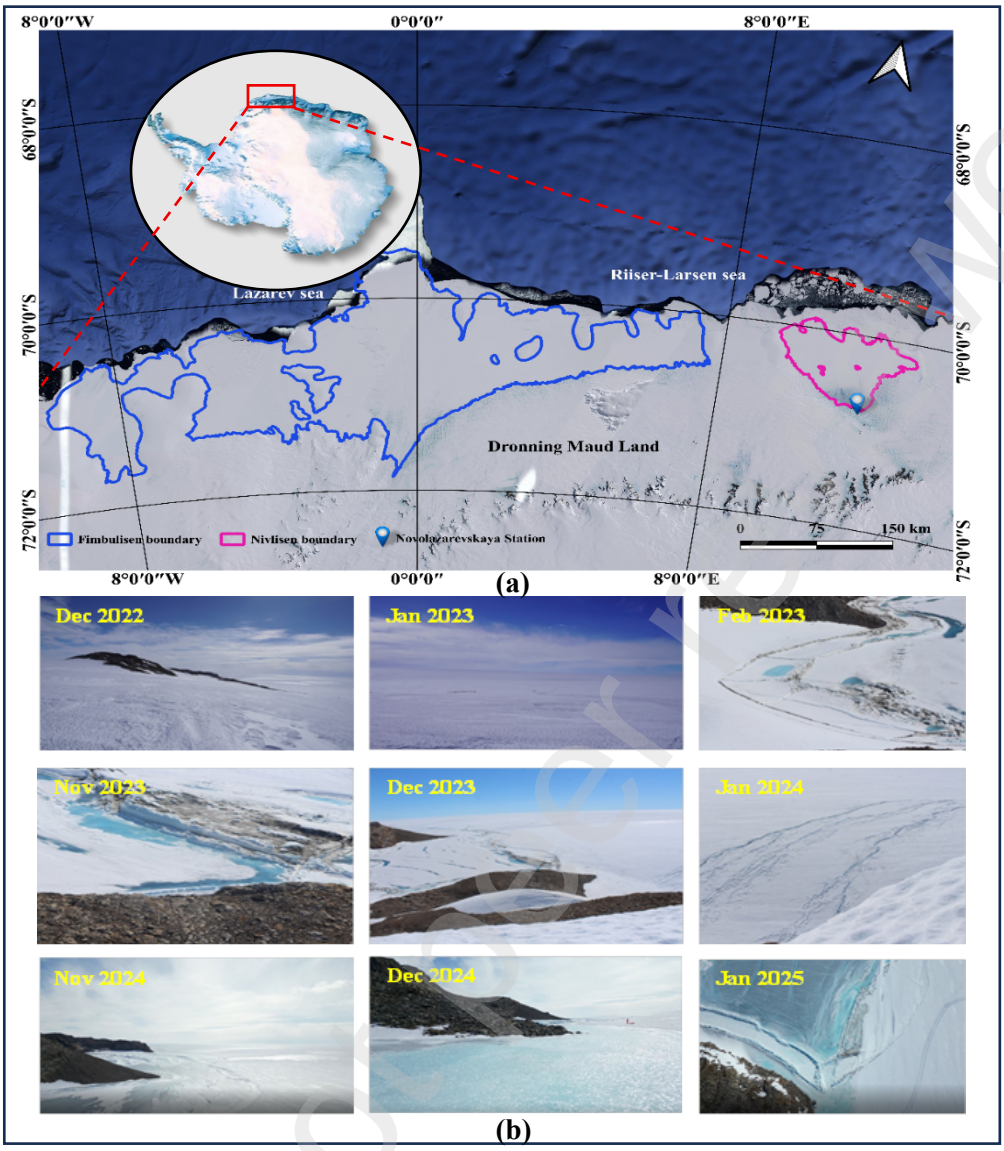

Figure 1. (a) Geographical Map showing study area (b) Field photograph of the Nivlisen Ice Shelf surface near Novo Station Grounding line, showing visible surface melt features (Photograph taken during Indian Scientific Expedition to Antarctica).

3. Data

The thermal model integrates atmospheric, glaciological, and oceanographic datasets to evaluate the long-term thermal evolution of the Nivlisen Ice Shelf (NIS). Surface-temperature forcing was derived from the ERA5 reanalysis record spanning 1940–2025, while ice thickness information was obtained from BedMachine Antarctica v4. A shelf-mean accumulation rate of 0.52 m ice eq. yr^{-1} derived from radar-based surface mass balance observations (Pratap et al., 2022) was used throughout the simulations. Additional datasets, including Novo automatic weather station observations, Circum-Antarctic Tidal Simulation (CATS) products, and the Fimbulisen S1 borehole temperature profile, were used for melt-metric calculations, uncertainty assessment, and regional model evaluation. Detailed dataset descriptions, processing procedures, quality-control criteria, and supporting analyses are provided in Supplementary Section S2. Six ice-thickness scenarios were derived from the

observed BedMachine Antarctica v4 thickness distribution to represent conditions ranging from the calving front to localized grounding-zone thickenings (Table 1). These scenarios were used to investigate the influence of ice thickness on thermal equilibration timescales and present-day thermal disequilibrium.

Throughout the simulations, present-day ice geometry, accumulation rate, and basal boundary conditions were held constant, while ERA5 surface-temperature forcing varied through time. The objective was to isolate the thermal response of the present-day NIS configuration to the observed atmospheric warming history rather than reconstruct past changes in ice-shelf geometry, accumulation rate, or ocean conditions.

Table 1. NIS ice-thickness scenarios derived from BedMachine Antarctica v4. Pe computed using acc = 0.52 m i.e. yr^{-1} (Pratap et al., 2022). τ = thermal equilibration timescale (Eq. 9). BM v4 = BedMachine Antarctica v4 (Morlighem et al., 2020).

Scenario	H (m)	Basis	Nodes	τ (yr)	Pe
Calving front	150	P5 BM v4	491	62	2
Thin shelf	180	P10 BM v4	521	90	3
Lower shelf	220	P25 BM v4	561	134	3
Mean shelf (PRIMARY)	312	Shelf mean	653	269	4
Thick zone	420	P75 BM v4	761	488	6
Grounding zone	600	P99 BM v4	941	995	9

Note: Scenarios were defined at the calving-front extreme (P5), two lower-quartile increments (P10, P25), the shelf mean, and two upper-quartile values (P75, P99) to sample the full observed thickness distribution asymmetrically, reflecting the positively skewed NIS thickness distribution in which the upper tail extends to localised grounding-zone thickenings substantially thicker than the median.

4. METHODS

The complete methodological workflow, including data acquisition, model development, thermal calculations, and statistical analyses, is summarised in Fig. 2.

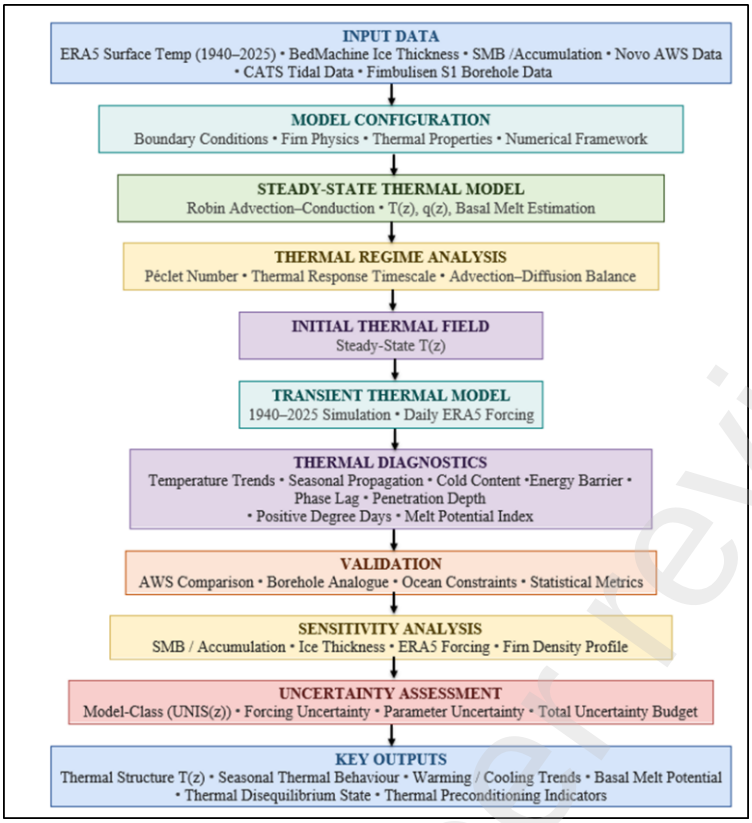

Figure 2. Integrated modelling framework combining Robin advection–conduction solutions, transient heat-transfer simulations, observational constraints, and uncertainty analyses to characterize the thermal regime of Nivlisen Ice Shelf.

4.1 Governing equations

4.1.1 Steady-state

The steady-state temperature profile, T(z), is governed by the one-dimensional advection–conduction equation of Robin, (1955):

$$k\frac{\partial^2 T}{\partial z^2} - \rho c_p \omega \frac{\partial T}{\partial z} = 0 \qquad (1)$$

where k=2.1 W $m^{-1}K^{-1}$ is the bulk thermal conductivity of ice (Cuffey and Patterson, 2010), ρ=900 kg m^{-3} is ice density, c_p=2009 J $kg^{-1}K^{-1}$ is specific heat capacity, and $\omega(z)$ is the vertical ice-velocity profile. Following Robin, (1955), downward advection associated with surface accumulation is represented by

$$\omega(z) = -acc\left(1 - \frac{z}{H}\right) \qquad (2)$$

where acc=0.52 m i.e. yr^{-1} is the shelf-mean accumulation rate and H is ice thickness. Equation (2) prescribes zero vertical velocity at the ice-shelf base (z=H) and maximum downward velocity at the surface (z=0), consistent with a floating ice shelf in approximate mass balance. The relative importance of advection and conduction is quantified using the Péclet number:

$$P_e = \frac{\rho c_p acc H}{k} \qquad (3)$$

For the primary thickness scenario (H=312 m), Eq. (3) yields Pe≈4. This indicates that conductive heat transport dominates the thermal regime while advection remains a secondary but non-negligible process. Accordingly, the steady-state temperature profile was computed using the full Robin, (1955) advection–conduction formulation represented by Eqs. (1)–(3).

4.1.2 Transient

The transient temperature evolution is governed by the one-dimensional heat diffusion equation:

$$\rho c_p \frac{\partial T}{\partial t} = k \frac{\partial^2 T}{\partial z^2} \quad (4)$$

where ρ=900 kgm^{-3} is ice density and c_p=2009 Jkg^{-1}K^{-1} is specific heat capacity. Equation (4) describes the propagation of time-varying thermal perturbations through the ice column by diffusion.

The transient formulation retains pure thermal diffusion and does not explicitly include an advection term. This simplification is adopted because the transient model is forced by observed surface-temperature variability and is designed to quantify the propagation of seasonal-to-decadal temperature anomalies into the firn and upper ice column. The advective contribution to year-to-year temperature anomalies is small relative to the diffusive propagation signal; the transient component is therefore well described by the heat diffusion equation alone, initialised from the Robin, (1955) advection–conduction steady-state profile (Eqs. 1–3). Consequently, the transient component represents departures from the steady-state profile arising from time-varying surface forcing. Because the transient analysis focuses on departures from the Robin, (1955) steady-state reference profile rather than on reconstruction of the full ice-column mass balance, accumulation-driven advection is treated as part of the background thermal structure established by Eqs. (1–3). For the primary scenario (Pe ≈ 4), advection influences the shape of the long-term equilibrium profile, whereas the transient formulation is designed specifically to examine the diffusive propagation of temperature anomalies about that reference state. The transient formulation therefore isolates the diffusive transmission of atmospheric temperature variability through the ice column while retaining the advection-controlled background state through the steady-state initial condition. The thermal diffusivity is given by

$$\alpha = \frac{k}{\rho c_p} = 1.16 * 10^{-6} m^2 s^{-1} \quad (5)$$

where α is the thermal diffusivity of ice. Equation (5) is used throughout the transient simulations.

4.2 Boundary conditions

The upper boundary condition for the steady-state model is T_s=−17.60°C, corresponding to the mean ERA5 surface skin temperature at the NIS centroid over 1940–2025. For the transient model, the daily ERA5 surface skin temperature is applied directly as the time-varying upper boundary condition at each timestep. The lower boundary condition is specified using the pressure-dependent seawater freezing temperature. Following (Fofonoff and Millard, 1983), the freezing-point temperature is given by

$$T_f = -0.0575S + 1.710523 * 10^{-3} S^{1.5} - 2.154996 * 10^{-4} S^2 - 7.53 * 10^{-4} P \quad (6)$$

where S is salinity (psu) and P is pressure (dbar). A salinity of S=34.5 psu, representative of Antarctic continental shelf waters (Jacobs, 1992), was adopted for all scenarios. Pressure was estimated from the ice draft assuming approximately 1 dbar per metre of seawater depth. Ice draft was calculated under hydrostatic equilibrium as

$$Draft = H\left(\frac{\rho}{\rho_w}\right) \quad (7)$$

where H is ice thickness, ρ=900 kgm^{-3} is ice density, and ρ_w=1028 kgm^{-3} is seawater density. Application of Eq. (6) yields freezing temperatures ranging from −1.90°C for the 150 m scenario (draft = 131 m) to −1.93°C for the 600 m scenario (draft = 525 m). The total variation across all thickness scenarios is only 0.03°C, comparable to the uncertainty associated with the assumed salinity (±0.5 psu corresponding to approximately ±0.03°C in Tf). Consequently, a uniform basal boundary condition of T_b=−1.90°C was adopted throughout the study. Scenario-specific T_b values were not retained because the 0.03°C inter-scenario range is below the salinity uncertainty of ±0.5 psu (~±0.03°C in Tf) and therefore unresolvable within the accuracy of the model. This assumption is consistent with the cold-water cavity conditions reported by Lindbäck et al., (2019), who observed no evidence of warm deep-water intrusion beneath NIS during 2017–2018.

4.3 Numerical scheme

4.3.1 Variable-resolution grid (steady-state)

The steady-state model employs a variable-resolution vertical grid designed to resolve the firn zone at high resolution while maintaining computational efficiency in the deeper ice. Zone 1 (0–30 m) uses a grid spacing of 0.10 m (301 nodes), Zone 2 (30–100 m) uses 0.50 m spacing (140 nodes), and Zone 3 (100 m–H) uses 1.00 m spacing. The total node count for the primary scenario (H = 312 m) is 653. The steady-state equations are solved using the Thomas algorithm (tridiagonal matrix solver) with harmonic-mean interface conductivities to ensure heat-flux continuity across zone boundaries. Variable grid spacing is handled using a second-order central finite-difference discretisation with asymmetric stencils at grid-transition interfaces.

4.3.2 Uniform 1 m grid (transient)

The transient model uses a uniform 1 m vertical grid (313 nodes for H = 312 m) to avoid numerical artefacts that may arise from abrupt grid-spacing transitions under time-varying surface forcing. The transient heat-diffusion equation (Eq. 4) is solved using an implicit backward-Euler scheme with a daily timestep (Δt=86,400 s). The backward-Euler formulation is unconditionally stable and permits efficient simulation of the full 1940–2025 forcing record. The transient model is initialised from the steady-state temperature profile interpolated onto the uniform grid.

4.4 Firn zone physics

The variable thermal properties of the firn zone are incorporated into the steady-state model through depth-dependent density and thermal-conductivity profiles. Firn densification is represented using the two-stage model of Herron and Langway, (1980), parameterised using the shelf-mean accumulation rate and mean surface temperature. Thermal conductivity is calculated from density using the Sturm et al., (1997) relationship

$$k(\rho) = 2.1\left(\frac{\rho}{917}\right)^{1.88} \quad (8)$$

where k is thermal conductivity (W m^{-1} K^{-1}) and ρ is density (kg m^{-3}). Below 80 m depth, where firn is assumed to have transitioned to near-solid ice density, constant bulk ice properties (k=2.1 $Wm^{-1}K^{-1}$, ρ=900 kgm^{-3}) are applied. Firn-property variations are incorporated into the steady-state temperature profile used to initialise the transient simulations. The transient model subsequently assumes constant bulk ice properties to maintain consistency with the uniform-grid transient formulation and to focus the analysis on the propagation of thermal anomalies through the bulk ice column.

4.5. Derived Metrics

All derived quantities were computed from the model temperature fields and atmospheric forcing data using the equations and definitions summarised in Supplementary Table 1. Thermal-gradient and seasonal-wave quantities derived from the temperature profiles include the vertical temperature gradient ($\partial T/\partial z$), temporal temperature change ($\partial T/\partial t$), seasonal amplitude, phase lag, and zero-curtain duration. Temperature curvature ($\partial^2 T/\partial z^2$) and heat-flux divergence ($\partial q/\partial z$) were evaluated from the steady-state profile only and are provided as supplementary diagnostic quantities in the accompanying data workbook. Heat-flux and thermal-energy quantities include conductive heat flux (q), thermal diffusivity (α), volumetric sensible heat (Qv), cold content (CC), column-integrated cold content (CC_{col}), column sensible heat (Q_{sens}), and rates of cold-content change. Additional thermal-wave metrics include seasonal penetration depth, amplitude damping, and thermal-wave velocity. Atmospheric melt metrics derived from the Novo AWS record include PDD (Annual PDD is numerically identical to Accumulated warmth (AW)), melt persistence index (MPI), melt onset, freeze onset, and zero-curtain duration. Primary model diagnostics include mid-column temperature, basal conductive heat flux, and conductive basal melt rate.

4.6 Péclet number and thermal timescale

The relative importance of advective and conductive heat transport was assessed using the Péclet number (Eq. 3). Thermal equilibration timescales were estimated as:

$$\tau = \frac{H^2}{\pi^2 \alpha} \quad (9)$$

where τ is the thermal equilibration timescale, H is ice thickness, and α is thermal diffusivity.

Equation (3) was evaluated for all thickness scenarios to quantify the relative importance of advection and conduction, whereas Eq. (9) was used to estimate the timescale over which the ice column approaches thermal equilibrium following a change in surface forcing. For the primary NIS scenario (H=312 m), Eq. (3) yields Pe=4, indicating that conductive heat transport dominates while accumulation-driven advection remains non-negligible. Equation (9) gives a thermal equilibration timescale of τ=269 yr, substantially longer than the 86-year ERA5 forcing record. The present thermal state should therefore be interpreted as a transient response superimposed on a longer-term adjustment toward equilibrium, while the steady-state solution provides a physically consistent reference state for evaluating thermal evolution.

4.7 Thermal preconditioning metrics

Four complementary sets of metrics were derived to characterise long-term changes in the thermal state of the NIS firn and near-surface ice column.

Approach 1 (Thermal preconditioning). Volumetric cold content was computed as

$$CC(z,t) = \frac{\rho c_p[0 - T(z,t)]}{10^6} \quad (10)$$

where CC is expressed in MJ m^{-3}. Annual cold-content values were evaluated at depths of 1, 2, 5, 10, 15, 20, and 30 m from the transient model output and integrated over the upper 30 m using the trapezoidal rule to obtain column cold content (MJ m^{-2}). The annual surface conductive heat flux was calculated as

$$q_{surf} = -k\frac{(T_{1m} - T_{surf})}{\Delta z} \quad (11)$$

where T_{1m} is the temperature at 1 m depth, T_{surf} is the surface temperature, and Δz=1 m. This quantity was used as a proxy for the conductive response of the near-surface ice column to atmospheric warming.

Approach 2 (Atmospheric melt metrics). PDD, melt onset day-of-year, freeze onset day-of-year, MPI, and zero-curtain duration were computed from the Novo AWS daily temperature record.

Approach 3 (Threshold analysis). Annual maximum ERA5 surface skin temperature was calculated for each year and analysed using ordinary least-squares (OLS) regression relative to the melt threshold of 0°C. The annual temperature deficit to the melting point was computed as

$$\Delta T_{melt} = 0°C - T_{max,\ annual} \quad (12)$$

where $T_{max,annual}$ is the annual maximum ERA5 surface skin temperature.

Approach 4 (Energy-barrier analysis). The energy barrier to surface melt was calculated as

$$E_{barrier} = \frac{\rho c_p |T_{s,\ mean}|}{10^6} \quad (13)$$

where $T_{s,mean}$ is the annual mean surface temperature. $E_{barrier}$ represents the energy required to warm 1 m^3 of surface ice to the melting point. Annual percentage changes relative to the 1940 baseline were used to quantify long-term reductions in resistance to surface melting.

The interpretation of these metrics recognises the limitations of ERA5 daily mean temperature as a direct predictor of surface melt. ERA5 daily mean temperatures represent grid-cell averages and do not resolve sub-grid spatial heterogeneity, short-duration radiative extremes, foehn-wind events, or melt-pond albedo feedbacks. The metrics defined above are therefore intended to characterise large-scale thermal variability rather than individual melt events.

4.8 Model-class error characterisation

In the absence of in-situ borehole temperature observations at NIS, structural uncertainty associated with the one-dimensional thermal model was characterised using the

Fimbulisen S1 borehole temperature profile (Humbert, 2010; Orheim et al., 1990) as a regional analogue. The same steady-state model formulation was applied using representative Fimbulisen parameters (H=400 m, T_s=−15.0°C, T_b=−2.0°C, and acc=0.10 m i.e. yr^{-1}). Model bias was computed as

$$B(z) = T_{model}(z) - T_{observed}(z) \quad (14)$$

where $T_{observed}$ is the borehole temperature profile. The NIS uncertainty envelope was estimated by mapping the Fimbul bias profile onto the NIS thickness domain using normalised depth and applying one-half of the absolute bias magnitude:

$$U_{NIS}(z) = \pm \frac{|B(z_{norm} * H_{NIS})|}{2} \quad (15)$$

where $z_{norm} = z / H_{Fimbul.}$ This approach is intended to provide a conservative estimate of model-class structural uncertainty. The large Fimbul biases are attributed primarily to unresolved ice-dynamic processes associated with the Jutulstraumen ice stream, particularly cold-core advection that cannot be represented within a one-dimensional vertical thermal model. Because these dynamic processes are not explicitly represented in the NIS model framework, the resulting uncertainty envelope is treated as a conservative estimate of model-class structural uncertainty. The Fimbul-derived uncertainty is therefore retained exclusively as a conservative structural error envelope and upper bound; it is not propagated as a probabilistic uncertainty estimate for NIS, and should not be interpreted as a transferable bias characterisation. This uncertainty characterisation follows the framework of Refsgaard et al., (2007) and should not be interpreted as direct validation of the NIS model results.

5. RESULTS

This section presents the steady-state and transient thermal characteristics of NIS, including its background thermal structure, seasonal thermal-wave behaviour, long-term thermal evolution, changes in cold-content storage, and indicators of thermal preconditioning. Results are interpreted within the framework of conductive–advective heat transfer and centennial-scale thermal adjustment. Model-class uncertainty was evaluated using the Fimbulisen S1 borehole analogue and is discussed in Supplementary Section S4.1.

5.1 Steady-state thermal structure of Nivlisen Ice Shelf

The steady-state advection–conduction model of (Robin, 1955) produces a non-linear vertical temperature structure for all six NIS thickness scenarios (Table 3; Fig. 3a). For the primary shelf-mean case (H = 312 m), the surface and basal boundary conditions are T_s = −17.60°C (1940–2025 ERA5 mean) and T_b = −1.90°C (pressure-melting point), respectively, with Pe = 4. Temperatures reach −15.47°C at 10 m, −12.74°C at 30 m, and −7.25°C at 100 m depth, while the geometric mid-depth temperature (z = 156 m) is T_{mid} = −4.86°C. The total column temperature range is 15.70°C, and integrated cold content is CC_{col} = 3001 MJ m^{-2} (Table 3; Fig. 3a). The vertical temperature gradient decreases with depth (Fig. 3b), from 0.305 °C m^{-1} at the surface to 0.162 °C m^{-1} at 10 m, 0.049 °C m^{-1} at 100 m, and 0.007 °C m^{-1} at the base. Correspondingly, conductive heat flux decreases from 134.8 mW m^{-2} in the firn layer to 14.22 mW m^{-2} at the ice base (Fig. 3c, d). Negative fluxes in the firn zone indicate upward conductive heat loss to the atmosphere, whereas the positive basal flux reflects upward oceanic heat input at the ice–ocean interface.

The conductive basal melt rate derived from q_{base} is Mb = 1.49 mm yr^{-1}, only 0.19% of the observed mean basal melt rate (~800 mm yr^{-1}) measured by autonomous phase-sensitive radar during 2017–2018 (Lindbäck et al., 2019), indicating that conductive melting is negligible relative to observed basal melt. Ice thickness strongly influences thermal conditions (Table 3; Fig. 3d). T_{mid} increases from −5.49°C for the 150 m calving-front scenario to −3.66°C for the 600 m grounding-zone scenario. Basal conductive heat flux decreases from 61.3 to 1.4 mW m^{-2}, while conductive melt rates decline from 6.44 to 0.15 mm yr^{-1} across the same thickness range. The Péclet number increases from 2 to 9, and the thermal equilibration timescale (τ) from 62 to 995 years, reflecting stronger advective influence and slower thermal adjustment in thicker ice shelves (Table 1). The thermal diffusivity profile records the firn–ice transition (Fig. 3e). Diffusivity increases from ~5.5 × 10^{-7} m^2 s^{-1} at the surface to ~8.5 × 10^{-7} m^2 s^{-1} at 30 m depth and converges below ~80 m to the bulk-ice value of 1.161 × 10^{-6} m^2 s^{-1}. Reduced diffusivity in the firn layer limits near-surface conductive heat transfer and influences seasonal thermal-wave propagation discussed in Section 5.2.

Table 3. Steady-state thermal characteristics of Nivlisen Ice Shelf for six BedMachine Antarctica v4 -derived ice-thickness scenarios, including mid-depth temperature, basal conductive heat flux, conductive basal melt rate, and basal temperature gradient. The shelf-mean thickness scenario (H = 312 m) is highlighted as the primary case.

Scenario	H (m)	T_{mid} (°C)	q_{base} (mWm^{-2})	M_b (mmyr^{-1})	$\partial T/\partial z\|_{base}$ (°C m^{-1})
Calving front	150	−5.49	61.3	6.44	0.0292
Thin shelf	180	−5.43	40.2	4.22	0.0191
Lower shelf	220	−5.32	26.8	2.81	0.0128
Mean shelf (PRIMARY)	312	−4.89	14.22	1.49	0.0068
Thick zone	420	−4.39	7.7	0.81	0.0037
Grounding zone	600	−3.66	1.4	0.15	0.0007

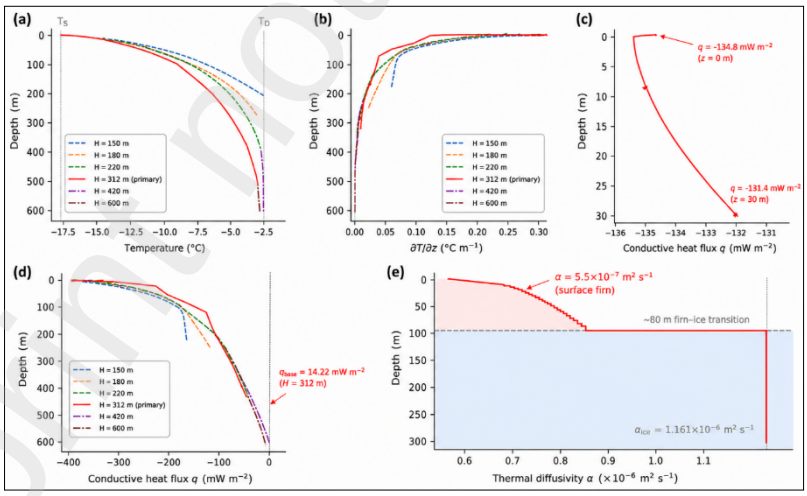

Figure 3. Steady-state thermal structure of Nivlisen Ice Shelf for six thickness scenarios. (a) vertical temperature profiles, (b) vertical temperature gradients, (c) near-surface conductive heat flux for the primary scenario (H = 312 m), (d) conductive heat flux through the full ice column, and (e) depth-dependent thermal diffusivity showing the firn–ice transition (~80 m). The primary scenario is shown in red.

5.2 Seasonal thermal-wave propagation

Seasonal surface-temperature forcing is rapidly attenuated within the NIS ice column (Fig. 4a, c). The characteristic e-folding penetration depth, $d = \sqrt{(2\alpha/\omega)}$, increases from 2.35 m at the surface ($\alpha \approx 5.5 \times 10^{-7}$ m² s⁻¹) to 3.42 m below ~80 m depth, where bulk-ice properties apply ($\alpha = 1.161 \times 10^{-6}$ m² s⁻¹). The ERA5 surface-temperature seasonal half-range (~9°C) is reduced to a seasonal amplitude of 0.58°C at 10 m depth, 0.042°C at 15 m, and <0.01°C below 20 m. Although the theoretical penetration depth is only 3.42 m, seasonal variability remains detectable to ~20 m (~6 penetration depths), beyond which the ice column is effectively decoupled from annual surface forcing (Fig. 4a,c; Carslaw and Jaeger, 1959; Paterson, 1994). The amplitude damping factor, $\exp(-z/d(z))$, declines from 0.660 at 1 m to 0.025 at 10 m and 0.0009 at 20 m (Fig. 4c). Consequently, only 2.5% of the surface signal remains at 10 m depth and <0.5% at 15 m. This strong attenuation reflects the low thermal diffusivity of the firn layer, where d(z) ranges from 2.35–2.93 m, substantially below the bulk-ice value of 3.42 m. The firn therefore acts as an effective thermal insulator, limiting seasonal heat penetration and preserving deeper ice from year-to-year surface variability (Hooke, 2019; Sturm et al., 1997; Zagorodnov et al., 2012).

Phase lag between the surface seasonal maximum and subsurface temperature maxima increases systematically with depth (Fig. 4b), reaching 24.2 days at 1 m, 112.5 days at 5 m, 213.3 days at 10 m, and 410 days at 20 m. Lags exceeding one year represent cumulative delays across successive seasonal cycles, indicating that the firn zone retains a multi-year memory of surface forcing. In contrast, the full ice column adjusts on the much longer thermal-equilibration timescale of $\tau = 269$ years (Cuffey and Clow, 1997; Dahl-Jensen et al., 1998; Humphrey and Echelmeyer, 1990). Thermal-wave velocity, $v(z) = d(z)\omega$, increases from 0.040 m day⁻¹ at the surface to 0.047 m day⁻¹ at 10 m and converges to the bulk-ice value of 0.059 m day⁻¹ (21.5 m yr⁻¹) below ~80 m (Fig. 4d). This corresponds to characteristic phase-propagation times of ~15 years to 100 m depth and ~270 years to the base of the 312 m column, closely matching the thermal-equilibration timescale ($\tau = 269$ years; Eq. 9, Table 1) and demonstrating the slow transmission of thermal perturbations through the ice shelf (Greve and Blatter, 2009). Overall, seasonal temperature forcing is largely confined to the upper ~20 m of the NIS column. Strong attenuation and increasing phase lag with depth cause temperatures below 10 m to integrate signals from multiple preceding years rather than the current season, providing substantial thermal buffering and separating long-term warming trends from seasonal variability (Fig. 4; Cuffey and Clow, 1997; Dahl-Jensen et al., 1998).

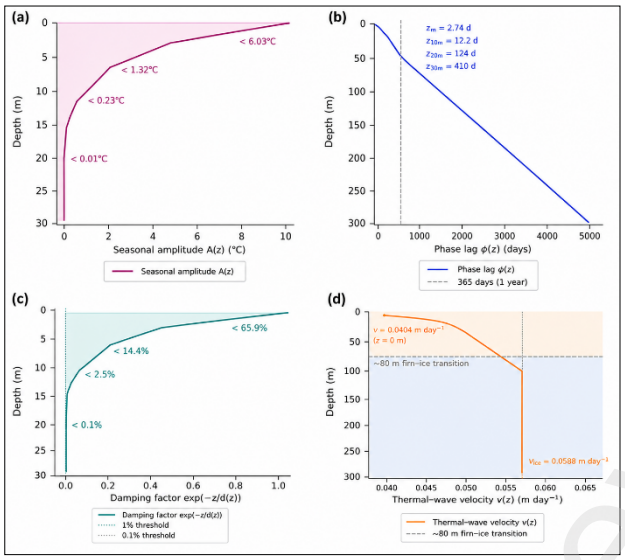

Figure 4. Seasonal thermal-wave characteristics of the NIS primary scenario (H = 312 m). (a) Seasonal temperature amplitude A(z) in the firn zone (0–30 m), (b) Phase lag between the surface seasonal maximum and the temperature maximum at depth across the full ice column (0–312 m), (c) Amplitude damping factor in the firn zone (0–30 m), (d) Thermal-wave velocity across the full ice column.

5.3 Transient thermal evolution (1940–2025)

ERA5 surface skin temperature at the NIS centroid exhibits a significant warming trend over 1940–2025 (Fig. 5a; Table 4). OLS regression yields a trend of +0.60 °C decade^{-1} (R^2 = 0.622, $p < 0.0001$, 95% CI ±0.10 °C decade^{-1}, n = 86 years), while annual maximum skin temperature increases at +0.12 °C decade^{-1} ($p = 0.0068$). The period-mean surface temperature is Ts = −17.60 °C, consistent with the steady-state boundary condition used in Section 4.2. Uncertainty associated with the pre-satellite ERA5 extension (1940–1978) is addressed in the uncertainty analysis. (Medley et al., 2017). The warming signal propagates downward with strong depth-dependent attenuation (Fig. 5b). Temperature trends decrease from +0.57 °C decade^{-1} at 1 m depth ($R^2 = 0.656$, $p < 0.0001$) to +0.31 °C decade^{-1} at 10 m depth ($R^2 = 0.659$, $p < 0.0001$), reflecting firn-layer damping quantified in Section 5.2. A transition from positive to negative trends occurs at approximately 27 m depth, with the sign reversal located between 25 and 30 m in the model output.

Below ~27 m, temperatures exhibit statistically significant cooling (Table 4; Fig. 5c). At 30 m depth, the trend is −0.05 °C decade^{-1} ($R^2 = 0.071$, $p = 0.013$), while at 100 m depth it reaches −0.23 °C decade^{-1} ($R^2 = 0.995$, $p < 0.0001$), corresponding to a total cooling of 1.84 °C between 1940 and 2025 (−7.26 °C to −9.09 °C). Although the 30 m trend explains only a modest fraction of variance, the sign reversal is physically consistent with the long thermal-equilibration timescale of the ice shelf (τ = 269 yr) (Robin, 1955). The near-perfect fit at 100 m indicates highly systematic, monotonic cooling of the deep column. The coexistence of near-surface warming and deep cooling reflects non-equilibrium thermal adjustment within a system whose equilibration timescale (τ = 269 yr) substantially exceeds the 86-year forcing record. Warming penetrates efficiently through the upper firn layer, whereas deeper ice remains dominated by slow adjustment toward the steady-state temperature structure. Consequently, cooling below ~27 m represents delayed equilibration of inherited thermal disequilibrium rather than downward propagation of a cooling atmospheric signal. The statistically significant sign

reversal—from warming above ~27 m to cooling below, is the principal finding of the transient analysis and demonstrates that the present-day NIS thermal profile remains out of equilibrium with recent atmospheric forcing (Fig. 5c; Table 4).

Table 4. OLS regression statistics for temperature trends at the ERA5 surface and four depths in the NIS primary scenario (H = 312 m) over 1940–2025 (n = 86 years). Temperature at depth from the transient model annual mean output. ERA5 skt = ERA5 surface skin temperature (Hersbach et al., 2020).

Variable	Trend (°C decade^{-1})	R^2	p-value	95 % CI (°Cdecade^{-1})	n
ERA5 T_s annual mean	+0.60	0.622	<0.0001	±0.10	86
ERA5 T_s annual max	+0.12	0.084	0.0068	±0.08	86
T at 1 m depth	+0.57	0.656	<0.0001	±0.09	86
T at 10 m depth	+0.31	0.659	<0.0001	±0.05	86
T at 30 m depth	−0.05	0.071	0.013	±0.04	86
T at 100 m depth	−0.23	0.995	<0.0001	±0.004	86

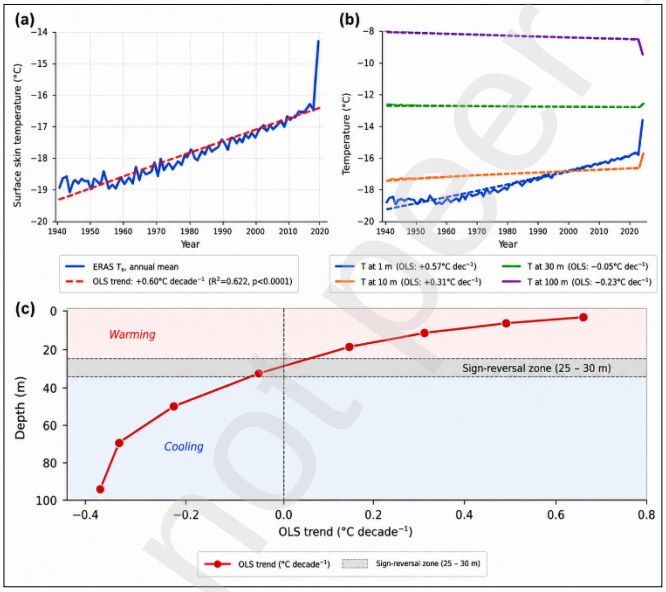

Figure 5. Transient thermal evolution of Nivlisen Ice Shelf (primary scenario, H = 312 m) forced by ERA5 surface skin temperature over 1940–2025. (a) ERA5 annual mean surface skin temperature at the NIS centroid. (b) Annual mean temperature evolution at four depths (1, 10, 30, and 100 m. (c) Depth profile of OLS trend slope from the surface (ERA5) to 100 m depth; vertical black line marks zero trend.

5.4 Thermal-energy evolution

Near-surface cold content declined substantially over the study period (Fig. 6a,b; Table 5). At 1 m depth, volumetric cold content decreased from 38.96 to 24.91 MJ m^{-2} between 1940 and 2025, a reduction of 14.05 MJ m^{-2} (36.1%), with an OLS trend of −1.04 MJ m^{-2} decade^{-1} (R^2 = 0.656, p < 0.0001). At 10 m depth, cold content decreased from 286.74 to 260.09 MJ m^{-2}, a reduction of 26.65 MJ m^{-2} (9.3%), corresponding to a trend of −5.64 MJ m^{-2} decade^{-1} (R^2 = 0.659, p < 0.0001). These trends mirror the warming observed at the same depths in

Section 5.3 and indicate a progressive reduction in the refreezing capacity of the near-surface firn column. In contrast, column-integrated cold content (CC_{col}) increased from 3557 to 3996 MJ m^{-2} between 1940 and 2025, an increase of 439 MJ m^{-2} (+12.3%), with an OLS trend of +49.3 MJ m^{-2} $decade^{-1}$ (R^2 = 0.840, p < 0.0001) (Fig. 6c; Table 5). The equivalent column sensible heat ($Q_{sens} = -CC_{col}$) evolved from −3557 to −3996 MJ m^{-2}, reaching a minimum of −4040 MJ m^{-2} in 2000 before partially recovering by 2025 (Fig. 6d). The transient 1940 CC_{col} value reflects anomalously cold ERA5 forcing in the first simulation year rather than the steady-state reference condition.

The contrasting behaviour of near-surface and column-integrated cold content is physically consistent. Near-surface depletion reflects atmospheric warming, whereas increasing CC_{col} results from continued cooling of the thermally dominant deep ice column (>30 m) on the long equilibration timescale (τ = 269 yr). Because the deep column contains substantially greater thermal mass than the near-surface firn, it dominates integrated energy metrics despite warming at the surface. The reduction in near-surface cold content provides the primary evidence for thermal preconditioning of NIS. The 36.1% decline at 1 m depth over 86 years represents a substantial and statistically robust decrease in the energy barrier to surface melt initiation, meltwater ponding, and persistence, with implications explored further in Section 5.5.

Table 5. Summary of thermal-energy evolution metrics for the NIS primary scenario (H = 312 m) over 1940–2025. The opposing signs of near-surface CC change (decreasing) and change (increasing) reflect the different depth scales of the warming and cooling signals documented in section 5.3.

Metric	1940	2025	Δ (absolute)	Δ (%)	OLS trend ($decade^{-1}$)	p-value
CC at 1 m (MJ m^{-3})	38.96	24.91	−14.05	−36.1 %	−1.04 MJ m^{-3}	<0.0001
CC at 10 m (MJ m^{-3})	286.74	260.09	−26.65	−9.3 %	−5.64 MJ m^{-3}	<0.0001
CC_{col} (MJ m^{-2})	3557	3996	+439	+12.3 %	+49.3 MJ m^{-2}	<0.0001

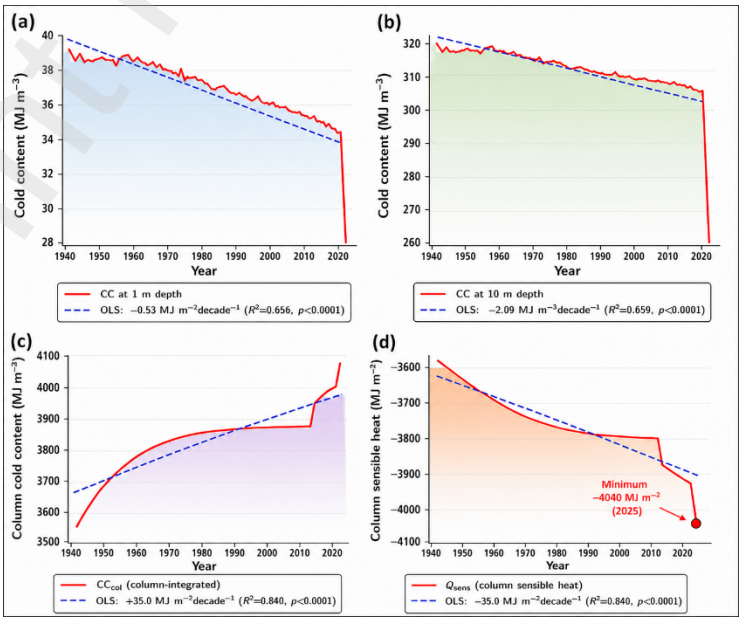

Figure 6. Thermal-energy evolution of Nivlisen Ice Shelf (primary scenario, H = 312 m) over 1940–2025. (a) Volumetric cold content at 1 m depth. (b) Volumetric cold content at 10 m depth. (c) Column-integrated cold content (d) Column sensible heat.

5.5 Atmospheric melt environment

Atmospheric melt indicators derived from the Novo AWS record provide observational context for the modeled thermal changes. Although positive degree days (PDD), melt potential index (MPI), melt onset, freeze onset, and zero-curtain duration indicate episodic melt-favourable conditions, no statistically significant long-term trends were detected during 1998–2025. The relatively short record and strong interannual variability limit trend detection. Detailed analyses are provided in Supplementary Section S3 (Supplementary Fig. S1; Supplementary Table T2). Consequently, assessment of thermal preconditioning relies primarily on the longer ERA5 record (1940–2025), which provides a more robust basis for evaluating multi-decadal thermal change at NIS.

5.6 Melt-threshold and energy-barrier analysis

Annual maximum ERA5 surface skin temperature increased from −2.89°C in 1940 to −0.61°C in 2025, with an OLS trend of +0.12 °C decade^{-1} (R^2 = 0.084, p = 0.007) despite substantial interannual variability (Fig. 7a). Annual maximum temperatures exceeded 0°C in only two years: 1971 (+0.47°C) and 1991 (+0.01°C). The temperature deficit to the melt threshold (ΔT_{melt}) declined from 2.89°C in 1940 to 0.61°C in 2025, a reduction of 2.28°C (78.8%), with an OLS trend of −0.12 °C decade^{-1} (p = 0.007) (Fig. 7b). Under a simple linear extrapolation of the historical trend, annual maximum temperatures would approach 0°C on a multi-decadal timescale; this estimate is illustrative only and does not constitute a climate projection (Fig. 7c).

The surface-melt energy barrier ($E_{barrier}$) decreased from 40.05 to 24.72 MJ m^{-3} between 1940 and 2025, a reduction of 15.33 MJ m^{-3} (38.3%), with an OLS trend of −1.09 MJ m^{-3} decade^{-1} (R^2 = 0.622, p < 0.0001) (Fig. 7d; Table 6). Relative to the 1940 baseline, $E_{barrier}$ had declined by 23.5% by 1980 and 32.7% by 2020, indicating progressive weakening of thermal resistance to melt over the study period. The five-year smoothed annual maximum temperature record (Fig. 7a) reveals decadal-scale variability superimposed on the long-term warming trend, with notable warm excursions in the early 1970s, mid-1990s, and after 2015. The smoothed series first exceeded −1.0°C around 2018, indicating that peak ERA5-derived surface thermal conditions are approaching levels capable of supporting near-surface melt under the sub-grid heterogeneity mechanisms discussed in Section 6.5. Together, the declining melt-threshold deficit and energy-barrier metrics provide quantitative evidence for progressive thermal preconditioning and reduced resistance to surface melt at NIS during 1940–2025.

Table 6. Summary of thermal-energy evolution and energy-barrier metrics for the NIS primary scenario (H = 312 m) over 1940–2025. The opposing signs of near-surface CC (decreasing) and CC_{col} (increasing) reflect different depth scales of warming and cooling.

Metric	1940	2025	Δ (absolute)	Δ (%)	OLS trend (decade⁻¹)	p-value
CC at 1 m (MJ m⁻³)	38.96	24.91	−14.05	−36.1 %	−1.04 MJ m⁻³	<0.0001
CC at 10 m (MJ m⁻³)	286.74	260.09	−26.65	−9.3 %	−5.64 MJ m⁻³	<0.0001
CC_{col} (MJ m⁻²)	3557	3996	+439	+12.3 %	+49.3 MJ m⁻²	<0.0001
$E_{barrier}$ (MJ m⁻³)	40.05	24.72	−15.33	−38.3 %	−1.09 MJ m⁻³	<0.0001

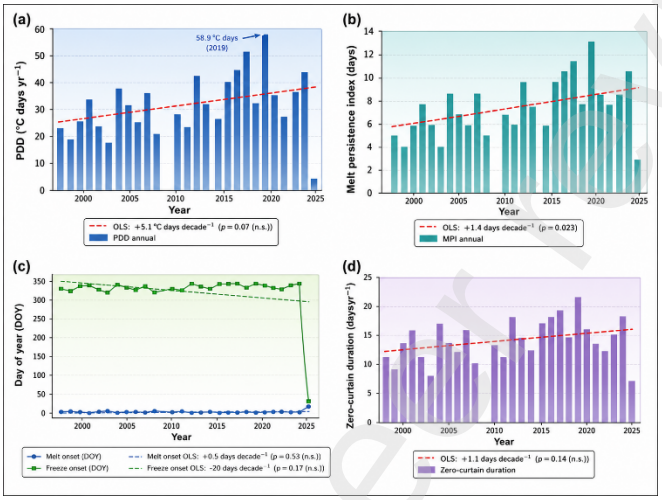

Figure 7. Melt-threshold and energy-barrier analysis for NIS (primary scenario, H = 312 m), 1940–2025. (a) ERA5 annual maximum surface skin temperature at the NIS centroid. (b) Temperature deficit to the 0°C melt threshold. (c) Linear extrapolation of the OLS trend to the 0°C threshold. (d) Energy barrier $E_{barrier}$ and percentage reduction from 1940 baseline (right axis, dash-dot green).

6. DISCUSSION

The present framework separates two related problems: (i) establishment of the background thermal structure through the Robin, (1955) advection–conduction solution and (ii) propagation of observed atmospheric temperature variability through that structure using a transient diffusion model. Consequently, the transient results should be interpreted as diffusive perturbations superimposed upon an advection-influenced thermal state rather than as a complete thermodynamic reconstruction of ice-shelf evolution.

6.1 Thermal regime of Nivlisen Ice Shelf in the Antarctic context

The thermal characterisation presented in Section 5.1 provides the first quantitative thermal baseline for NIS and places its thermal regime within the broader Antarctic ice-shelf context. For the primary scenario, T_{mid} = −4.86°C, q_{base} = 14.22 mW m⁻², Pe = 4, and τ = 269 yr. Comparisons with selected Antarctic ice shelves are provided in Supplementary Table 3, although published thermal profiles remain scarce for East Antarctic shelves (Humbert, 2010; Holland et al., 2015; Pattyn, 2018). Pe and τ values reported for comparison shelves were estimated from published thickness and accumulation data using Eqs. 3 and 9. The closest analogue is Fimbulisen (Dronning Maud Land), where a two-dimensional thermal model constrained by the S1 borehole was presented by Humbert, (2010). Fimbulisen has a lower

accumulation rate (~0.10 m i.e. yr^{-1}) and Pe = 1, indicating a more conduction-dominated regime than NIS (Orheim et al., 1990). Its S1 profile is additionally influenced by cold-core advection from Jutulstraumen, a process absent at NIS. The estimated equilibration timescale for Fimbulisen (H = 400 m) is ~442 yr, longer than the NIS value of 269 yr, implying that both shelves remain out of thermal equilibrium with recent forcing (Robin, 1955). At the colder end of the Antarctic spectrum, the Ross Ice Shelf experiences interior surface temperatures of approximately −24 to −28°C (Cuffey and Paterson, 2010) and very low basal melt rates (0–0.3 m yr^{-1}). The NIS conductive basal melt rate of 1.49 mm yr^{-1} is consistent with this broader cold-water cavity setting (Rignot at al., 2013; Depoorter, et al., 2013). The nearby Roi Baudouin Ice Shelf experiences similar atmospheric forcing and accumulation rates (0.40–0.60 m i.e. yr^{-1}), suggesting a comparable Péclet-number regime and predominantly shallow, seasonally driven basal melting. Likewise, the Amery Ice Shelf is a cold-water cavity system influenced primarily by High-Salinity Shelf Water and Antarctic Surface Water, with mean basal melt rates of ~0.42 m yr^{-1} (Galton-Fenzi et al., 2012; Wen et al., 2010).

The most distinctive characteristic of NIS is its intermediate Pe = 4, whereas many cold-water cavity East Antarctic shelves exhibit Pe < 2. This places NIS in a regime where conduction remains dominant but advection exerts a measurable influence, increasing sensitivity to both atmospheric forcing and ice-column structure (Greve and Blatter, 2009). Because the equilibration timescale (τ = 269 yr) greatly exceeds the 86-year ERA5 record, the present thermal state reflects both recent surface warming and inherited colder conditions at depth. The coexistence of a shallow warming layer above a deeper cooling layer therefore indicates that NIS remains in a thermally non-equilibrium state (Dahl-Jensen et al., 1998). By providing the first quantitative thermal baseline for NIS, this study fills an important gap in East Antarctic ice-shelf characterisation. Unlike Fimbulisen (Humbert, 2010), Ross, and Amery, NIS has remained largely uncharacterised despite documented melt-pond occurrence and its proximity to the Novo and Maitri research stations. The thermal baseline established here provides a benchmark for future thermistor observations, satellite-derived surface-temperature products, and coupled ice–ocean modelling studies.

6.2 Seasonal thermal-wave behaviour and firn buffering

The seasonal-wave analysis demonstrates that atmospheric forcing is confined to the upper ~20 m of the NIS ice column, where seasonal temperature amplitudes decay to <0.01 °C (Section 5.2). Ice below this depth is effectively decoupled from annual surface variability, indicating that the thermal preconditioning documented in Section 5.4 is driven by multi-decadal warming rather than individual seasonal cycles (Cuffey and Clow, 1997; Dahl-Jensen et al., 1998). This confinement results from the low thermal diffusivity of the firn layer. Surface firn diffusivity ($\alpha \approx 5.5 \times 10^{-7}$ m^2 s^{-1}) is approximately half the bulk-ice value (1.161×10^{-6} m^2 s^{-1}), yielding a seasonal penetration depth of only 2.35 m at the surface compared with 3.42 m in bulk ice. Correspondingly, the amplitude attenuation coefficient is greater in firn (0.43 m^{-1}) than in ice (0.29 m^{-1}), causing seasonal signals to decay ~1.5 times more rapidly and effectively insulating the deeper column from year-to-year atmospheric variability (Carslaw and Jaeger, 1959; Cuffey and Paterson, 2010; Sturm et al., 1997). Large phase lags further demonstrate the thermal memory of the firn layer. Seasonal maxima lag the surface by 213 days at 10 m depth and 410 days at 20 m depth, indicating that temperatures within the lower firn integrate atmospheric forcing from previous years rather than the current season. Consequently, future

thermistor observations at NIS should extend over multiple years to distinguish long-term warming trends from seasonal variability (Zagorodnov et al., 2012).

The strong contrast between the seasonal penetration depth (~20 m) and the full-column equilibration timescale (τ = 269 yr) highlights two distinct thermal regimes within NIS. Seasonal thermal waves propagate rapidly ($v = 0.059$ m day^{-1}) but remain restricted to the firn layer, whereas long-term thermal evolution is controlled by the slow diffusion of multi-decadal forcing through the full ice column. This separation justifies treating seasonal variability and long-term thermal adjustment independently (Sections 5.2 and 5.3). These findings are consistent with classical thermal-wave theory and previous studies of firn thermal buffering in polar ice masses (Carslaw and Jaeger, 1959; Cuffey and Paterson, 2010; Zagorodnov et al., 2012). The principal implication is that seasonal atmospheric warming does not significantly influence temperatures below ~20 m; therefore, the cold-content depletion and energy-barrier reduction identified in Section 5.4 represent long-term structural thermal change rather than interannual variability.

6.3 Evidence for long-term thermal preconditioning and non-equilibrium adjustment

The transient and thermal-energy analyses (Sections 5.3–5.4) reveal an apparent paradox: ERA5 surface temperatures warmed at +0.60 °C decade^{-1} ($p < 0.0001$) and near-surface cold content declined by 36.1% since 1940, yet the deep ice column (>30 m) cooled systematically, with T_{100m} decreasing at −0.23 °C decade^{-1} ($R^2 = 0.995$). This behaviour reflects thermal preconditioning, defined here as the progressive reduction of the near-surface cold reservoir and melt-energy barrier due to sustained atmospheric warming. Thermal preconditioning does not imply that melt or hydrofracture has occurred; rather, it indicates reduced resistance to future melt initiation. The apparent paradox is explained by the thermal equilibration timescale of NIS (τ = 269 yr), which is 3.1 times longer than the 86-year ERA5 forcing record. Because the forcing record represents only ~32% of τ, recent warming has primarily affected the upper firn column, whereas temperatures below ~30 m remain dominated by long-timescale equilibration processes (Cuffey and Paterson, 2010). Consequently, near-surface warming and deep-column cooling are simultaneous manifestations of a thermally non-equilibrium system. This structure is reflected in the cold-content metrics (Fig. 8). Near-surface cold content decreased by 36.1% at 1 m depth and 9.3% at 10 m depth, while column-integrated cold content (CC_{col}) increased by 12.3%. The increase in CC_{col} arises because the thermally dominant deep column continues to cool during equilibration and therefore requires more energy to reach the melting point. As a result, CC_{col} should not be interpreted as an indicator of melt susceptibility; the relevant metrics are near-surface cold content and the melt-energy barrier ($E_{barrier}$).

The near-unit linearity of the T_{100m} trend (R^2 = 0.995) further supports this interpretation. The observed 1.84 °C cooling at 100 m depth between 1940 and 2025 is consistent with slow diffusive adjustment operating over a fraction of the equilibration timescale, indicating that deep-column thermal evolution will continue for decades to centuries irrespective of short-term atmospheric variability (Bell et al.,, 2018; Robin, 1955; Wessem et al., 2018). For ice-shelf stability, the operationally relevant signal is the depletion of the near-surface thermal buffer. Since 1940, cold content at 1 m depth has declined by 36.1% and $E_{barrier}$ by 38.3%, reducing the capacity of the firn column to absorb and refreeze meltwater. These metrics therefore quantify the degree of thermal preconditioning, whereas deep-column

cooling primarily provides evidence for persistent non-equilibrium thermal adjustment. This framework is consistent with observations of enhanced melt activity at NIS. Surface melt rates of ~80 mm w.e. yr^{-1} were reported by (Trusel et al., 2013), and expansion of melt ponds and supraglacial lakes after 2015 was documented by (Geetha Priya et al., 2023). Progressive firn densification toward ~900 kg m^{-3} by ~80 m depth further reduces meltwater storage capacity and may influence the balance between refreezing, retention, and ponding (Jakobs et al., 2020; Lenaerts et al., 2017). Consequently, a firn column that has lost 36.1% of its 1940 cold content possesses a substantially reduced thermal buffer against meltwater persistence and pond development.

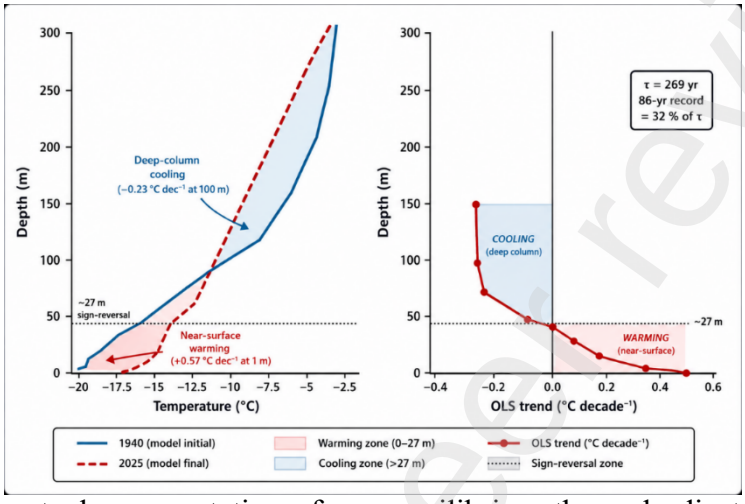

Figure 8. Conceptual representation of non-equilibrium thermal adjustment in Nivlisen Ice Shelf during 1940–2025. Left: modelled temperature profiles showing near-surface warming and deep-column cooling separated by a sign-reversal depth (~27 m). Right: depth-dependent temperature trends, highlighting the transition from warming in the upper firn layer to cooling at depth.

6.4 Atmospheric melt environment at NIS

The absence of statistically significant trends in the Novo AWS melt metrics during 1998–2025 does not contradict the long-term ERA5 warming trend identified for 1940–2025. The Novo record spans only 27 years (~31% of the ERA5 period), and the high interannual variability of PDD (coefficient of variation ~77%) substantially reduces statistical power for trend detection (Refsgaard et a., 2007). Consequently, the lack of significant trends in the AWS record is consistent with warming that becomes detectable only over the longer ERA5 time series. A further limitation is the ~53 km separation between Novo station (70.77°S, 11.86°E) and the NIS centroid. As a continental inland station, Novo records regional atmospheric conditions rather than local ice-shelf surface temperatures. Localised processes including warm-air advection, mesoscale variability, albedo contrasts between ponded and dry firn, and topographic airflow channelling may generate melt conditions on NIS that are not captured by the station record (Gossart et al., 2019; König-langlo and Loose, 2007). Thus, Novo AWS data characterise the regional melt environment, whereas ERA5 and satellite observations provide broader spatial context.

Although annual maximum ERA5 temperatures remained below freezing in most years, they increased at +0.12 °C $decade^{-1}$ ($p = 0.007$), reducing the temperature deficit to the melt threshold from 2.89°C in 1940 to 0.61°C in 2025. Small positive excursions above ERA5 grid-

cell mean temperatures may still occur during short-lived radiation events or warm-air advection episodes capable of producing localized surface melt (Trusel et al., 2013; Wessem et al., 2018). The Novo record nevertheless documents episodic melt-favourable conditions during the period of observed melt-pond expansion after 2015. Mean annual PDD increased from 25.3 °C days yr^{-1} (1998–2014) to 33.9 °C days yr^{-1} (2015–2025), MPI reached 13 consecutive positive-temperature days in 2019, and freeze onset was delayed to DOY 366 in several recent years. Although these changes are not statistically significant, they are qualitatively consistent with the declining thermal resistance to melt identified in Section 5.6 and the post-2015 expansion of melt ponds reported by(Geetha Priya et al., 2023). Overall, the Novo AWS and ERA5 datasets provide complementary perspectives on the atmospheric melt environment. Novo captures year-to-year variability and episodic melt-favourable conditions, including PDD values up to 58.9 °C days yr^{-1}, whereas the 86-year ERA5 record provides the more robust evidence for long-term warming at the NIS centroid (Gossart et al., 2019; Hersbach et al., 2020).

6.5 Surface melt despite predominantly sub-freezing ERA5 temperatures

ERA5 daily mean surface skin temperatures at the NIS centroid remained below 0°C in all but two years of the 1940–2025 record (1971 and 1991), yet surface melt, melt ponds, and supraglacial lakes are well documented at NIS (Geetha Priya et al., 2023,2024; Trusel et al., 2013). This apparent contradiction arises because ERA5 grid-cell daily mean temperatures are not equivalent to local surface conditions. Therefore, the absence of ERA5 temperatures above 0°C does not imply the absence of local surface melt. ERA5 represents area-averaged conditions at 0.25° (~28 km) resolution and provides daily mean skin temperatures rather than point-scale or sub-daily extremes (Hersbach et al., 2020). The NIS region contains a mixture of ice shelf, coastal terrain, and ocean, allowing local temperatures to deviate substantially from grid-cell means. Brief melt-producing temperature excursions may therefore occur without appearing in the daily ERA5 record. One mechanism is episodic warm-air advection from the continental interior, which can generate foehn-like temperature anomalies several degrees above the regional mean(König-langlo and Loose, 2007; Lenaerts et al., 2016; Nicolas et al., 2017). Such events may persist for only hours to days, making them difficult to detect in daily mean ERA5 data. The Novo AWS, located ~53 km from the NIS centroid, may partially capture these episodes, including years with PDD values as high as 58.9 °C days yr^{-1}.

A second mechanism is radiative heating of the snow and ice surface. During austral summer, incoming solar radiation at 70°S can exceed 400 W m^{-2}, enabling surface temperatures to reach the melting point even when air temperatures remain below zero(van den Broeke et al., 2011). Low-albedo surfaces such as blue ice, refrozen pond ice, or impurity-rich snow absorb more energy than surrounding firn. Once meltwater forms, the melt–albedo feedback becomes important because liquid water (albedo ~0.06) absorbs substantially more radiation than fresh snow (albedo ~0.80), promoting further melt and pond expansion (Tedesco et al., 2011; Bell et al., 2018,; Wessem et al., 2018). Topographic depressions provide a third mechanism by concentrating meltwater from both local and upslope sources (Banwell et al., 2013; Geetha Priya et al., 2023; Bell et al., 2018). Ponded water absorbs additional solar energy and enhances melting of pond margins and bases. Satellite observations further demonstrate active meltwater routing and drainage-channel connectivity across NIS, indicating that lateral transfer of meltwater between depressions occurs during melt events (Langley et al., 2011). Independent observations confirm that surface melt at NIS is both recurrent and increasing.

(Trusel et al., 2013) estimated melt rates of ~80 mm w.e. yr^{-1}, among the highest in central Dronning Maud Land, while Geetha Priya et al. (2023,2024) documented post-2015 expansion of melt ponds and supraglacial lakes, including events exceeding 1 km^2. The thermal preconditioning identified in this study, a 36.1% reduction in near-surface cold content and a 38.3% reduction in $E_{barrier}$, provides a quantitative explanation for why such melt-favourable conditions have become increasingly effective at generating and sustaining surface melt despite predominantly sub-freezing ERA5 temperatures (Bell et al., 2018).

6.6 Thermal-mechanical implications for Nivlisen Ice Shelf

The depletion of the near-surface thermal buffer documented in Sections 5.4 and 5.6 has important implications for NIS stability. Since 1940, volumetric cold content at 1 m depth has declined by 36.1% and the melt-energy barrier ($E_{barrier}$) by 38.3%, meaning substantially less atmospheric energy is now required to initiate surface melting. Although these changes do not directly generate meltwater, they lower the energetic threshold for melt onset, persistence, and accumulation, thereby creating conditions increasingly favourable for surface melt (Kuipers et al.,2014; Bell et al., 2018). A related consequence is the reduction in firn refreezing capacity. As near-surface cold content decreases, less meltwater can be refrozen before the firn becomes saturated. Combined with progressive densification toward ~900 kg m^{-3} by ~80 m depth, which reduces available pore space, this limits the capacity of the firn column to retain meltwater and promotes ponding or deeper percolation. Such conditions are commonly associated with the onset of melt-pond development on Antarctic ice shelves (Banwell et al., 2013; Kuipers et al., 2014; Bell et al., 2018; Scambos et al., 2000).

Observations from NIS are consistent with this thermal trajectory. Trusel et al. (2013) reported surface melt rates of ~80 mm w.e. yr^{-1}, while Geetha Priya et al. (2023) documented recurring melt ponds and supraglacial lakes after 2015, including events exceeding 1 km^2. By the mid-2010s, both $E_{barrier}$ and near-surface cold content had already undergone substantial depletion relative to their 1940 baselines, indicating a weakened thermal buffer against meltwater accumulation. The strongest link between the thermal state identified here and potential structural impacts is provided by the LEFM analysis of Geetha Priya et al., (2026, preprint), which reported stress-intensity factors exceeding published fracture-toughness ranges at several supraglacial ponds, including a system-wide drainage response during January 2026. The present study does not model fracture mechanics or infer hydrofracture occurrence; however, a firn column that has lost 36.1% of its near-surface cold content and 38.3% of its melt-energy barrier provides a physically plausible thermal setting for the persistence of meltwater loads capable of enhancing fracture propagation (Alley et al.,2016; van der Veen, 2007). These results support a thermal–mechanical pathway in which sustained atmospheric warming depletes the near-surface cold reservoir, reduces resistance to melt initiation, promotes persistent meltwater accumulation, and increases the likelihood of hydraulic loading within fractures. While each stage is supported by independent evidence (Banwell et al., 2013; Scambos et al., 2000), this study specifically quantifies the thermal preconditioning stage. Thermal preconditioning should nevertheless be viewed as a necessary rather than sufficient condition for instability. The presence of surface melt does not imply imminent hydrofracture or ice-shelf collapse. Instead, the significance of this study lies in quantifying, for the first time, the magnitude and rate of thermal change at NIS since 1940 and demonstrating that this evolution is consistent with conditions associated with melt-pond

development and hydrofracture susceptibility elsewhere in Antarctica (Banwell et al., 2013; Bell et al., 2018; Scambos et al., 2000).

7. Conclusions

This study presents the first quantitative thermal characterisation of NIS, central Dronning Maud Land, East Antarctica, using a one-dimensional heat-transfer framework forced by ERA5 temperatures over 1940–2025. For the primary scenario (H = 312 m), the ice shelf is characterised by T_{mid} = −4.86 °C, q_{base} = 14.22 mW m^{-2}, a conductive basal melt rate of 1.49 mm yr^{-1}, Pe = 4, and a thermal equilibration timescale of τ = 269 yr. Seasonal atmospheric forcing is confined to the upper ~20 m of the firn column, whereas deeper ice responds on centennial timescales. Transient simulations reveal a thermally non-equilibrium system. Surface temperatures warmed at +0.60 °C decade^{-1} during 1940–2025, while temperatures at 100 m depth cooled at −0.23 °C decade^{-1} (R^2 = 0.995), producing a sign-reversal depth of ~27 m. This coexistence of near-surface warming and deep-column cooling reflects the fact that the 86-year forcing record is substantially shorter than the equilibration timescale, leaving the deeper ice column in long-term adjustment to past climatic conditions. The most important consequence of this evolution is progressive thermal preconditioning of the near-surface firn. Since 1940, cold content at 1 m depth has decreased by 36.1%, $E_{barrier}$ by 38.3%, and the temperature deficit to the melt threshold by 78.8%. These changes quantify a substantial reduction in the thermal buffer available to absorb and refreeze meltwater. Although column-integrated cold content increased because of continued deep-column cooling, the near-surface metrics most relevant to melt susceptibility show significant depletion. The results further demonstrate that surface melt can occur despite predominantly sub-freezing ERA5 temperatures through the combined effects of sub-grid atmospheric variability, warm-air advection, radiative heating, melt–albedo feedbacks, and topographic controls on meltwater accumulation. The quantified thermal preconditioning therefore provides a physically consistent framework for interpreting the documented expansion of melt ponds and indications of hydrofracture susceptibility previously reported for NIS. Overall, NIS is undergoing progressive thermal preconditioning while remaining in a state of long-term thermal disequilibrium. The thermal baseline established here fills a major knowledge gap for East Antarctic ice shelves and provides a quantitative benchmark for future borehole observations, satellite monitoring, and coupled ice–ocean modelling studies aimed at understanding the future thermal and structural evolution of Antarctic ice shelves.

Acknowledgement:

The authors gratefully acknowledge the continued encouragement and dedicated support of our Director and the Sri Sringeri Sharada Peetham, Sringeri, whose unwavering commitment to scientific research and polar science has been instrumental in enabling this work. The authors further acknowledge the support rendered by PTICL and TITCL toward the successful completion of this research. The authors also acknowledge the scientific community, data centres, and international agencies that maintain and freely provide high-quality observational, reanalysis, and geospatial datasets, without which studies of remote polar environments would not be possible. The authors acknowledge the logistical support provided by the National Centre for Polar and Ocean Research (NCPOR), Ministry of Earth Sciences (MoES), Government of India, under the 42nd, 43rd and 44th Indian Scientific Expedition to Antarctica

(ISEA) through projects 42-AMOS/OR-06(2) and 44-RSG/OR-01(2), which facilitated Antarctic field activities and the acquisition of field photographs used in this study.

Declaration of Generative AI and AI-assisted technologies in the writing process:

During the preparation of this manuscript, the authors used AI-assisted language tools to improve the clarity and readability of the text. All scientific content, analyses, interpretations, and conclusions were developed and verified by the authors. The authors carefully reviewed and edited all AI-assisted outputs and accept full responsibility for the content of the published work.

Data Availability Statement:

This study does not involve custom code or proprietary algorithms. All datasets used are publicly available. In-situ firn and ice temperature profile data for Fimbul ice shelf were obtained from Humbert et al. (2010) as archived in the original publication. Meteorological data for Novolazeravskaya were accessed from Meteostat (https://meteostat.net/). Ice-shelf tidal and oceanographic data were obtained from the CATS (Circum-Antarctic Tidal Simulation) model, available through the United States Antarctic Program Data Center (USAP-DC) at https://www.usap-dc.org. ERA5 reanalysis data were accessed from the Copernicus Climate Data Store (CDS) at https://cds.climate.copernicus.eu/ . Bedrock topography and ice thickness data were obtained from BedMachine Antarctica Version 4 (Morlighem et al., 2020), available from the National Snow and Ice Data Center (NSIDC) at https://nsidc.org/data/nsidc-0756/versions/3 . All data supporting the findings of this study are included in the manuscript and its supplementary materials.

Author contributions: GP- Conceptualisation, methodology, formal analysis, Writing-original draft, reviewing and editing, DJ and AS -reviewing and editing

Competing interest:

All the authors declare they have no conflict of interest.

References

1. A. Gossart and S. Helsen,J. T. M. Lenaerts,S. Vanden Broucke,N. P.M. Van Lipzig, A. N. S. (2019). An evaluation of surface climatology in state-of-the-art reanalyses over the Antarctic Ice Sheet. *Journal of Climate*, *32*(20), 6899–6915. https://doi.org/10.1175/JCLI-D-19-0030.1
2. Abhishek Bamby Alphonse, Marzena Osuch, John Mohd Wani, N. H. (2026). An integrated computational framework for high-dimensional parameter optimization in coupled hydro-thermal permafrost modelling. *Cold Regions Science and Technology*, *248*(January), 104950. https://doi.org/10.1016/j.coldregions.2026.104950
3. Alley, K., Scambos, T., Siegfried, M. et al. (2016). Impacts of warm water on Antarctic ice shelf stability through basal channel formation. *Nature Geoscience*, *9*, 290–293. https://doi.org/10.1038/ngeo2675
4. B. K. Galton-Fenzi, J. R. Hunter, R. Coleman, S. J. Marsland, and R. C. W. (2012). Modeling the basal melting and marine ice accretion of the Amery Ice Shelf. *Journal of Geophysical Research: Oceans*, *117*(9), 1–19. https://doi.org/10.1029/2012JC008214
5. Banwell, A. F., Macayeal, D. R., & Sergienko, O. V. (2013). Breakup of the Larsen B Ice Shelf triggered by chain reaction drainage of supraglacial lakes. *Geophysical*

Research Letters, *40*, 1–5. https://doi.org/10.1002/2013GL057694
6. C. J.van der Veen. (2007). Fracture propagation as means of rapidly transferring surface meltwater to the base of glaciers. *Geophysical Research Letters*, *34*(1), 1–5. https://doi.org/10.1029/2006GL028385
7. Catherine Walker,Joanna Millstein,Bertie Miles,Sue Cook,Alexander Fraser,Andreas Colliander,Sidharth Misra,Luke Trusel,Susheel Adusumilli, H. A. F. (2024). The Multi-decadal Collapse of East Antarctica ' s Conger-Glenzer Ice Shelf. *Nature Geoscience*, *17*, 1240–1248. https://doi.org/doi.org/10.1038/s41561-024-01582-3
8. Cuffey, K. M., & Clow, G. D. (1997). Temperature, accumulation, and ice sheet elevation in central Greenland through the last deglacial transition. *Holocene*, *102*(C12), 26,383-26,396. https://doi.org/doi.org/10.1029/96JC03981
9. Dahl-Jensen, D., Mosegaard, K., Gundestrup, N., Clow, G. D., Johnsen, S. J., Hansen, A. W., & Balling, N. (1998). Past temperatures directly from the Greenland Ice Sheet. *Science*, *282*(5387), 268–271. https://doi.org/10.1126/science.282.5387.268
10. Deva Jefflin, A. R., Geetha Priya, M., Nasar, D., Singh, S. K., & Oza, S. (2024). Estimation of Mass Balance of Baspa Basin, Western Himalayas Using Remote Sensing Data. *Communications in Computer and Information Science*, *2030*, 205–217. https://doi.org/10.1007/978-3-031-53731-8_17
11. E. Rignot, S. Jacobs, J. Mouginot, B. S. (2013). Ice-Shelf Melting Around Antarctica. *Science*, *341*(6143), 266–270. https://doi.org/10.1126/science.1235798
12. Geetha Priya M, Charu Prabha R P, Y Mallikarjuna Madhav, Adithya Sunil, Raina Bharathi, Deva Jefflin A R (2026). *Decadal Evolution of Supraglacial Hydrology on the Nivlisen Ice Shelf : From Localized Ponding to Spatially Synchronized Hydrofracture Forcing* (Vol. 4). https://doi.org/10.3390/rs15245676
13. Geetha Priya M, Raghavendra K R, Dhanush S, Rakshita C, M. B. and Deva Jefflin A R. (2024). Monitoring of melt ponds and supra-glacial lakes over Nivlisen Ice Shelf, East Antarctica, using satellite-based multispectral data. *Civil Engineering Innovations for Sustainable Communities with Net Zero Targets*, 297–308. https://doi.org/10.1201/9781032686899-24
14. Greve, R., & Blatter, H. (2009). Dynamics of Ice Sheets and Glaciers. In *Advances in Geophysical and Environmental Mechanics and Mathematics*.
15. Hersbach, H., Bell, B., Berrisford, P., Hirahara, S., Horányi, A., Nicolas, J., Peubey, C., Radu, R., Bonavita, M., Dee, D., Dragani, R., Flemming, J., Forbes, R., Geer, A., Hogan, R. J., Janisková, H. M., Keeley, S., Laloyaux, P., Cristina, P. L., & Thépaut, J. (2020). The ERA5 global reanalysis. *Quarterly Journal Ofthe Royal Meteorological Society*, *146*(730), 1999–2049. https://doi.org/10.1002/qj.3803
16. Horatio Scott Carslaw, J. C. J. (1959). *Conduction of Heat in Solids*. Clarendon Press.
17. Humbert, A. (2010). The temperature regime of Fimbulisen, Antarctica. *Annals of Glaciology*, *51*(55), 56–64. https://doi.org/10.3189/172756410791392673
18. Humphrey, N., & Echelmeyer, K. (1990). Hot-water drilling and bore-hole closure in cold ice. *Journal of Glaciology*, *36*(124), 287–298. https://doi.org/https://www.cambridge.org/core/journals/journal-of-glaciology/article/hotwater-drilling-and-borehole-closure-in-cold-ice/CC42F47A681A3A76E9283643C4F8AC41
19. Jacobs, S. (1992). Is the Antarctic ice sheet growing? *Nature*, *360*, 29–33. https://doi.org/10.1038/360029a0
20. Jakobs, C. L., & , Carleen H. Reijmer, C. J. P. Paul Smeets, Luke D. Trusel , Willem Jan van de Berg1, M. R. van den B. and J. M. van W. (2020). A benchmark dataset of in situ Antarctic surface melt rates and energy balance. *Journal of Glaciology*, *66*(256), 1–12. https://doi.org/10.1017/jog.2020.6

21. Jens Christian Refsgaard , Jeroen P. van der Sluijs, Anker Lajer Højberg, P. A. V. (2007). Uncertainty in the environmental modelling process A framework and guidance. *Environmental Modelling & Software*, *22*(11), 1543–1556. https://doi.org/10.1016/j.envsoft.2007.02.004
22. K.M. Cuffey, W. S. B. P. (2010). The Physics of Glaciers Fourth Edition. In *Elsevier* (Vol. 4).
23. König-langlo, G., & Loose, B. (2007). The Meteorological Observatory at Neumayer Stations (GvN and NM-II) Antarctica. *Polarforschung*, *76*(1–2), 25–38. http://hdl.handle.net/10013/epic.28566.d001
24. Krishna Venkatesh, Deva Jefflin A R, Adithya Sunil, & G. P. M. (2026). A Scalable Borehole Thermometry Framework for Process-Based Monitoring of Near- Surface Thermal Dynamics Across Polar and High-Mountain Cryosphere Systems . *Distribution*, 1–23. http://classtap.pbworks.com/f/SkillSoft+-+Blended+Elearning.pdf
25. Langley, K., Kohler, J., Matsuoka, K., Sinisalo, A., Scambos, T., Neumann, T., Muto, A., Winther, J.-G., & Albert, M. (2011). Recovery Lakes, East Antarctica: Radar assessment of sub-glacial water extent. *Geophysical Research Letters*, *38*(5). https://doi.org/10.1029/2010GL046094
26. Lenaerts, J., Lhermitte, S., Drews, R. et al. (2017). Meltwater produced by wind–albedo interaction stored in an East Antarctic ice shelf. *Nature Climate Change*, *7*, 58–62. https://doi.org/10.1038/nclimate3180
27. Lenaerts, J. T. M., Lhermitte, S., Drews, R., Ligtenberg, S. R. M., Berger, S., & Helm, V. (2016). Meltwater produced by wind – albedo interaction stored in an East Antarctic ice shelf. *Nature Climate Change*, *7*, 1–6. https://doi.org/10.1038/NCLIMATE3180
28. Lindbäck, K., Moholdt, G., Nicholls, K. W., Hattermann, T., Pratap, B., Thamban, M., & Matsuoka, K. (2019). Spatial and temporal variations in basal melting at Nivlisen ice shelf, East Antarctica, derived from phase-sensitive radars. *Cryosphere*, *13*(10), 2579–2595. https://doi.org/10.5194/tc-13-2579-2019
29. M. A. Depoorter, J. L. Bamber, J. A. Griggs, J. T. M. Lenaerts, S. R. M. Ligtenberg, M. R. van den B. & G. M. (2013). Calving fluxes and basal melt rates of Antarctic ice shelves. *Nature*, *502*(7469), 89–92. https://doi.org/10.1038/nature12567
30. M. Tedesco, X. Fettweis, M. R. van den Broeke, R. S. W. van de Wal, C. J. P. P. Smeets, W. J. van de Berg, M.C. Serreze and, J. E. B. (2011). The role of albedo and accumulation in the 2010 melting record in Greenland. *Environmental Research Letters*, *6*(1), 167–186. https://doi.org/10.1088/1748-9326/6/1/014005
31. Mathieu Morlighem, Eric Rignot, Tobias Binder, Donald Blankenship, Reinhard DrewS, Graeme Eagles, Olaf Eisen, Fausto Ferraccioli, Ren´e Forsberg, Pe- ter Fretwell, Vikram Goel, Jamin S. Greenbaum, Hilmar Gudmundsson, Jingxue GUO, Veit Helm, Coen Hofsted, D. Y. (2020). Deep glacial troughs and stabilizing ridges unveiled be- neath the margins of the Antarctic ice sheet. *Nature Geoscience*, *13*, 132–137. https://doi.org/10.1038/s41561-019-0510-8
32. Medley, B., Mcconnell, J. R., Neumann, T. A., Reijmer, C. H., Chellman, N., Sigl, M., & Kipfstuhl, S. (2017). Temperature and Snowfall in Western Queen Maud Land Increasing Faster Than Climate Model Projections. *Geophysical Research Letters*, *45*, 1–9. https://doi.org/10.1002/2017GL075992
33. Michael M. Herron and Chester C. Langway. (1980). Firn densification: an empirical model. *Journal of Glaciology, 25*(93). https://doi.org/10.3189/S0022143000015239
34. Murugesan, G. P., Koppuram Ramesh Babu, R., Baineni, M., Chidananda, R., Satish, D., Sivalingam, S., Aruldhas, D. J., Venkatesh, K., Muniswamy, N. K., & Luis, A. J. (2023). Decoding the Dynamics of Climate Change Impact: Temporal Patterns of

Surface Warming and Melting on the Nivlisen Ice Shelf, Dronning Maud Land, East Antarctica. *MDPI Remote Sensing*, *15*(24), 1–21. https://doi.org/10.3390/rs15245676
35. N. P. Fofonoff and R.C. Millard Jr., & Endorsed. (1983). Algorithms for computation of fundamental properties of seawater. *Unesco Technical Papers in Marine Scierlce*, *44*, 1–53.
36. Nicolas, J. P., Vogelmann, A. M., Scott, R. C., Wilson, A. B., Cadeddu, M. P., Bromwich, D. H., Verlinde, J., Lubin, D., Russell, L. M., Jenkinson, C., Powers, H. H., Ryczek, M., Stone, G., & Wille, J. D. (2017). January 2016 extensive summer melt in West Antarctica favoured by strong El Niño. *Nature Communications*, *8*(May), 1–10. https://doi.org/10.1038/ncomms15799
37. Orheim, O., Hagen, J.O., Österhus, S. and Sætrang, A. C. (1990). Studies on, and underneath, the ice shelf Fimbulisen. *Nor. Polarinst. Medd.*, *113*, 59–73. https://hdl.handle.net/11250/4631965
38. P. R. Holland, A. Brisbourne, H. F. J. Corr, D. McGrath, K. Purdon, J. Paden, H. A. Fricker, F. S. Paolo, and A. H. F. (2015). Oceanic and atmospheric forcing of Larsen C Ice-Shelf thinning. *Cryosphere*, *9*(3), 1005–1024. https://doi.org/10.5194/tc-9-1005-2015
39. Pattyn, F. (2018). The paradigm shift in Antarctic ice sheet modelling. *Nature Communications*, *9*(1), 10–12. https://doi.org/10.1038/s41467-018-05003-z
40. Peter Kuipers Munneke, Stefan R.M. Ligtenberg, Michiel R. Van Den Broeke, D. G. V. (2014). Firn air depletion as a precursor of Antarctic ice-shelf collapse. *Journal of Glaciology*, *60*(220), 205–214. https://doi.org/10.3189/2014JoG13J183
41. Pratap, Bhanu, Rahul Dey , Kenichi Matsuoka, G. M., & Lindbäck, Katrin, Vikram Goel, C. M. L. and M. T. (2022). Three-decade spatial patterns in surface mass balance of the Nivlisen Ice Shelf, central Dronning Maud Land, East Antarctica. *Journal of Glaciology*, *68*(267), 174–186. https://doi.org/10.1017/jog.2021.93
42. Robin E. Bell, Alison F. Banwell, L. D. T. J. K. (2018). Antarctic Surface Hydrology and Impacts on Ice Sheet Mass Balance 2. *Nature Climate Change*, *8*, 1044–1052. https://doi.org/doi.org/10.1038/s41558-018-0326-3
43. Robin, G. de Q. (1955). Ice Movement and Temperature Distribution in Glaciers and Ice Sheets. *Cambridge University Press*, *2*(18), 523–532. https://doi.org/10.3189/002214355793702028
44. Roger LeB.Hooke. (2019). *Principles of Glacier Mechanics* (Vol. 1).
45. Scambos, T. A., Hulbe, C., Fahnestock, M., & Bohlander, J. (2000). The link between climate warming and break-up of ice shelves in the Antarctic Peninsula. *Journal OfGlaciology*, *46*(1996), 516–530. https://doi.org/10.3189/172756500781833043
46. Sturm, M., Holmgren, I. J. O. N., Nig, I. M. A. X. K. O., Morris, K. I. M., Cold, R., Box, P., Wainwright, F., & Us, A. (1997). The thertnal conductivity of seasonal snow. *Journal of Glaciology*, *43*(143), 26–41. https://doi.org/10.3189/S0022143000002781
47. Trusel, L. D., Frey, K. E., Das, S. B., Munneke, P. K., Trusel, L. D., Frey, K. E., Das, S. B., & Munneke, P. K. (2013). Satellite-based estimates of Antarctic surface meltwater fluxes Satellite-based estimates of Antarctic surface meltwater fl uxes. *Geophysical Research Letters*, *40*, 6148–6153. https://doi.org/10.1002/2013GL058138
48. W. S. B. Paterson. (1994). *The physics of glaciers. 3rd edition.* Pergamon. https://doi.org/10.1016/C2009-0-14802-X
49. Wen, J., Wang, Y., Wang, W., Jezek, K. C., Liu, H., & Allison, I. (2010). Basal melting and freezing under the Amery Ice Shelf, East Antarctica. *Journal of Glaciology*, *56*(195), 81–90. https://doi.org/10.3189/002214310791190820
50. Wessem, J. M. Van, Berg, W. J. Van De, Noël, B. P. Y., Meijgaard, E. Van, Amory,

C., Birnbaum, G., Jakobs, C. L., Krüger, K., Lenaerts, J. T. M., Lhermitte, S., Ulft, L. H. Van, Wouters, B., Wuite, J., & Broeke, M. R. Van Den. (2018). Modelling the climate and surface mass balance of polar ice sheets using RACMO2 – Part 2 : Antarctica (1979 – 2016). *The Cryosphere*, *12*, 1479–1498. https://doi.org/10.5194/tc-12-1479-2018

51. Zagorodnov, V., Nagornov, O., Scambos, T. A., Muto, A., Mosley-Thompson, E., Pettit, E. C., & Tyuflin, S. (2012). Borehole temperatures reveal details of 20th century warming at Bruce Plateau, Antarctic Peninsula. *The Cryosphere*, *6*(3), 675–686. https://doi.org/10.5194/tc-6-675-2012

Supplementary Material

Warming above, cooling below: First model-based quantitative thermal-regime assessment and subsurface thermal evolution of Nivlisen Ice Shelf, East Antarctica, revealing non-equilibrium thermal adjustment and progressive thermal preconditioning

Geetha Priya M*, Deva Jefflin A R, Adithya Sunil

Centre for Incubation, Innovation, Research and Consultancy, Jyothy Institute of Technology, Bengaluru-560082.

*geetha.sri82@gmail.com

S1. Detailed Study Area Characteristics

This section provides additional information on the Nivlisen Ice Shelf geometry, surface mass balance, basal melting environment, and documented surface melt processes that support the thermal modelling framework used in this study.

S1.1 Location and geometry

The NIS is located in central Dronning Maud Land (cDML) along the Princess Astrid Coast of East Antarctica. It lies seaward of the Schirmacher Oasis at approximately 70.3°S, 11.3°E and is flanked by the Leningradkollen and Djupranen ice rises, which exert orographic control on the surface mass balance distribution (Pratap et al., 2022). The shelf is characterised by slow ice flow velocities and moderate ice thickness, with a BedMachine Antarctica v4 mean thickness of 311.49 m (this study) and a spatial standard deviation of 124.8 m. Ice thickness ranges from ~146 m near the calving front (P5 percentile) to >600 m in localised grounding-zone thickenings (P99 = 603 m). The total shelf area is approximately 7,228 km².

S1.2 Surface mass balance

The surface mass balance (SMB) of NIS is characterised by a strong east-west gradient, with local variations spanning 1–2 orders of magnitude across the shelf (Pratap et al., 2022). The shelf-mean SMB derived from shallow ice-penetrating radar over full-coverage periods (1999–2017) is 0.52 ± 0.057 m i.e. yr^{-1} (four periods; Pratap et al., 2022; Table 1). This value is used as the accumulation rate input to the thermal model.

S1.3 Basal melting and ocean cavity

Lindbäck et al., (2019) characterised basal melt at NIS using autonomous phase-sensitive radars during 2017–2018. Annually averaged melt rates are moderate (~0.8 m yr^{-1}), with seasonal variability near the ice front driven by summer-warmed ocean surface water rather than warm deep-water intrusion. At 35 km into the cavity (ice draft 280 m), melt rates are lower (~0.4 m yr^{-1}) with no seasonality. These observations indicate that NIS behaves as a cold-water cavity shelf, a characterisation that is consistent with the basal temperature boundary condition adopted in this study and with the relatively weak conductive heat fluxes obtained from the thermal model.

S1.4 Surface melt and supraglacial hydrology

Surface melt at NIS is well established. Trusel et al., (2013) estimated NIS surface melt rates at ~80 mm w.e. yr^{-1} from satellite radar backscatter, representing the second-highest rate in cDML. Geetha Priya et al., (2023)documented melt pond and supraglacial lake dynamics over 2000–2023, identifying a consistent increase in melt extent and lake formation post-2015. Geetha Priya et al., (2023) characterised temporal patterns of surface warming and melting using Landsat and Sentinel-1 data. The surface melt observed at NIS occurs despite ERA5 daily mean skin temperatures remaining below 0°C at the grid-cell scale, highlighting the importance of sub-grid spatial heterogeneity associated with peak radiative forcing, foehn wind events, and melt–albedo feedbacks that are not resolved by ERA5 0.25° daily mean output.

S2. Data Sources, Processing, and Model Inputs

S2.1 ERA5 surface skin temperature

The ERA5 reanalysis surface skin temperature (skt) was extracted for the NIS centroid grid point (70.25°S, 11.25°E; nearest to shelf centroid 70.3°S, 11.3°E) from the Copernicus Climate Data Store (CDS) for the period 1940 January 1 to 2025 December 31 (Hersbach et al., 2020). ERA5 standard reanalysis was used in preference to ERA5-Land, which is invalid over floating ice shelf grid cells. Hourly data were resampled to daily means. The pre-satellite era (1940–1978) uses the ERA5 Back Extension, which assimilates fewer observations and carries larger uncertainty than the post-1979 period (Hersbach et al., 2020). Nevertheless, the extended record provides a temporally consistent forcing dataset for evaluating multi-decadal thermal evolution, while the implications of pre-1979 uncertainty are considered in the uncertainty assessment. The extracted record contains 31,412 daily values with zero missing days and zero null values, spanning an 86-year forcing period. The 1940–2025 mean skin temperature is $T_s = -17.60$°C, used as the steady-state upper boundary condition.

S2.2 Ice thickness — BedMachine Antarctica v4

Ice thickness was extracted from BedMachine Antarctica v4 (Morlighem et al., 2020) at 500 m resolution (EPSG (European Petroleum Survey Group) :3031). The shelf-mean thickness of 311.49 m was derived from QGIS (Quantum Geographic Information System) analysis of all valid pixels within the NIS boundary and is adopted as the primary model thickness (H = 312 m after rounding). Calving-front extraction yielded a mean + 0.5σ thickness of 144 m (→150 m), and the full pixel percentile distribution was used to define the remaining five thickness scenarios rounded to the nearest 10s except primary scenario (312 m). The six thickness scenarios were selected to represent the observed range of NIS ice thickness from the calving front to localised grounding-zone thickenings.

S2.3 Accumulation rate

The shelf-mean accumulation rate was derived from (Pratap et al., (2022), Table 1), who conducted shallow ice-penetrating radar sounding across ~400 km of profiles on NIS and over the adjacent ice rises. The mean of four full-coverage periods (1999–2017) is 0.517 m i.e. yr^{-1}, rounded to acc = 0.52 m i.e. yr^{-1} = 0.48 m w.e. yr^{-1} for use in the model. The stated measurement uncertainty is ±11% Pratap et al., (2022) . Two earlier periods (1986–1999) were excluded from the mean because they were derived from limited spatial coverage.

S2.3.1 Assumptions regarding temporal consistency

The thermal model combines an 86-year ERA5 surface-temperature forcing record (1940–2025) with present-day geometric and boundary-condition datasets, including BedMachine Antarctica v4 ice thickness, the shelf-mean accumulation rate from Pratap et al., (2022), and the cold-water cavity characterisation of Lindbäck et al., (2019). These quantities are held constant throughout the simulation period. This approach is intended to isolate the thermal response of the present-day NIS configuration to the observed surface-temperature

history and does not attempt to reconstruct historical changes in ice-shelf geometry, accumulation rate, or ocean conditions.

S2.4 Novo AWS

Daily temperature observations from Novo station (WMO (World Meteorological Organization) 89512; 70.77°S, 11.86°E) were obtained from Meteostat (https://meteostat.net/en/) for the period 1973–2025. The station is located approximately 53 km from the NIS centroid. Novo data are used exclusively as an atmospheric forcing proxy for melt-metric calculations (positive degree days, melt onset, freeze onset, melt persistence index, and zero-curtain duration) and are not used as forcing for the thermal model.

A longer monthly-mean temperature record is available from the SCAR READER (scientific Committee on Antarctic Research Reference Antarctic Data for Environmental Research) database beginning in 1961; however, monthly data do not permit computation of daily melt metrics and were therefore not used in this study.

Data quality for the Meteostat daily record was assessed using annual record coverage. Years with fewer than 200 daily observations were excluded. Consequently, melt-metric calculations and trend analyses were restricted to the period 1998–2025, for which annual data coverage satisfied the quality-control threshold.

S2.5 CATS tidal data

Tidal constituent information for the NIS region was obtained from the Circum-Antarctic Tidal Simulation (CATS) model, following Padman et al., (2002). The CATS dataset used in this study contains 49,930 spatial records covering ten tidal constituents. The dominant constituent is M2 (maximum amplitude 0.244 m), with a form factor $F = (K1 + O1)/ (M2 + S2) = 0.679$, indicating a mixed, mainly semi-diurnal tidal regime. The CATS-derived tidal constituents are used to characterise the regional tidal environment and to estimate the potential influence of tidal variability on the basal boundary condition. In the uncertainty analysis, tidal variability contributes the seventh uncertainty source (±0.025°C on the basal boundary condition, T_b).

S2.6 Fimbulisen S1 borehole

The Fimbulisen S1 borehole temperature profile (Humbert, 2010; Orheim et al., 1990) provides 18 depth–temperature pairs spanning 0–395 m. No openly archived digital version of this profile was identified in PANGAEA, SCAR, or Norwegian Polar Institute data repositories. The profile is used exclusively for regional model-class error characterisation and does not constitute direct validation of NIS results.

Supplementary Table 1. Derived quantities, equations, units, and references used in the NIS thermal-regime analysis.

Category	Quantity	Symbol	Unit	Equation / Definition	Reference
Primary Model Outputs	Steady-State Temperature Profile	T(z)	°C	$k\partial^2T/\partial z^2 - \rho c_p\, w\partial T/\partial z = 0$, $w(z)=-acc(1-z/H)$	Robin (1955)
Primary Model Outputs	Transient Temperature Evolution	T(z,t)	°C	$\rho c_p \partial T/\partial t = k\partial^2T/\partial z^2$	Cuffey & Paterson 2010
Temperature gradients	Vertical temperature gradient	$\partial T/\partial z$	°C m^{-1}	$[T(z+\Delta z) - T(z-\Delta z)]/(2\Delta z)$	Standard finite difference
Temperature gradients	Temperature curvature	$\partial^2T/\partial z^2$	°C m^{-2}	$[T(z+\Delta z) - 2T(z) + T(z-\Delta z)]/\Delta z^2$	Standard finite difference
Temperature gradients	Temporal Temperature change	$\partial T/\partial t$	°C Day^{-1}	$[T(t) - T(t-\Delta t)]/\Delta t$	Standard finite difference
Seasonal metrics	Seasonal amplitude	A(z)	°C	$A_{surf} \times \exp(-z/d(z))$	Carslaw & Jaeger (1959)
Seasonal metrics	Phase lag	φ(z)	days	$z/(d(z)\times\omega\times 86400)$	Carslaw & Jaeger (1959)
Seasonal metrics	Zero-curtain duration	t_{zc}	days yr^{-1}	Days per year with $\lvert T_{Novo}\rvert \leq 0.5$°C	Lachenbruch et al., 1988
Heat flux	Conductive heat flux	q	W m^{-2}	$q = -k\,\partial T/\partial z$	Fourier's law
Heat flux	Heat-flux divergence	$\partial q/\partial z$	mW m^{-3}	$-k\,\partial^2T/\partial z^2$	Fourier's law
Thermal properties	Thermal diffusivity	α	m^2 s^{-1}	$k/(\rho c_p)$	Cuffey & Paterson (2010)
Thermal energy	Volumetric sensible heat	Q_v	MJ m^{-3}	$\rho c_p T /10^6$	Cuffey & Paterson (2010)
Thermal energy	Cold content	CC	MJ m^{-3}	$\rho c_p(0-T)/10^6$	Cuffey & Paterson (2010)
Thermal energy	Column cold content	CC_{col}	MJ m^{-2}	$\int_0^H CC(z)\,dz$	This study
Thermal energy	Column sensible heat (time series)	Q_{sens}	MJ m^{-2}	$Q_{sens} = \rho c_p/10^6 \times \int_0^H T(z,t)dz$	Cuffey & Paterson 2010;
Thermal	Rate of cold-	d(CC)/dt	MJ m^{-2} yr^{-1}	$-\rho c_p\,\partial T/\partial t /10^6$	This study

energy	content change				
Thermal-wave metrics	Penetration depth	d	m	$d = \sqrt{(2\alpha/\omega)}$	Carslaw & Jaeger (1959)
Thermal-wave metrics	Amplitude damping	damp(z)	—	$\exp(-z/d)$	Carslaw & Jaeger (1959)
Thermal-wave metrics	Thermal-wave velocity	$v_{thermal}$	m day^{-1}	$d\omega$	Carslaw & Jaeger (1959)
Melt metrics	Positive degree days	PDD	°C days yr^{-1}	$\Sigma \max(T,0)$	Hock (2003)
Melt metrics	Melt persistence index	MPI	days	Maximum consecutive days with T > 0°C	This study
Melt metrics	Melt onset	$_{Tm}$	DOY	First day with T > 0°C	This study
Melt metrics	Freeze onset	T_f	DOY	Last day with T > 0°C	This study
Threshold metrics	Temperature deficit to melt threshold	ΔT_{melt}	°C	$0°C - T_{max,annual}$	This study
Threshold metrics	Energy barrier to surface melt	$E_{barrier}$	MJ m^{-3}	$\rho c_p \lvert T_{s,mean}\rvert / 10^6$	This study
Model diagnostics	Mid-column temperature	T_{mid}	°C	T(H/2)	This study
Model diagnostics	Basal conductive heat flux	q_{base}	mW m^{-2}	Basal value of Fourier heat flux	Fourier's law
Model diagnostics	Conductive basal melt rate	M_b	mm yr^{-1}	$q_{base}/(\rho L_f)$	Cuffey & Paterson (2010)
Uncertainty metrics	Fimbul bias profile	B(z)	°C	$T_{model} - T_{obs}$	Refsgaard et al. (2007)
Uncertainty metrics	NIS uncertainty envelope	$U_{NIS}(z)$	°C	$\pm \frac{\lvert B(z_{norm} * H_{NIS})\rvert}{2}$	Refsgaard et al. 2007

Note: Because temperatures remain below 0°C throughout the model domain, $CC_{col} = -Q_{sens}$. Both quantities are defined for completeness; subsequent analysis focuses primarily on CC_{col} as a measure of the thermal energy deficit relative to the melting point.

S3. Atmospheric melt metrics

Atmospheric melt metrics were computed from daily temperature observations at Novo station (WMO 89512; 70.77°S, 11.86°E), located approximately 53 km from the NIS centroid (Meteostat, 2024). These metrics are derived exclusively from the Novo AWS record and are independent of the thermal model output. Following data-quality screening (Supplementary section S2.4), trend analysis is restricted to the 27 good-quality years spanning 1998–2025.

Annual PDD at Novo ranged from 4.0 to 58.9 °C days yr^{-1} over the 1998–2025 record, with a period mean of approximately 28 .5°C days yr^{-1} (Supplementary Figure 1a, Supplementary Table 2). The 2019 austral summer recorded the maximum observed PDD of 58.9 °C days yr^{-1} and falls within the period of enhanced melt-pond occurrence reported at NIS after 2015 (Geetha Priya et al., 2023). The OLS trend over 1998–2025 is +5.6 °C days $decade^{-1}$, but this trend is not statistically significant ($R^2 = 0.085$, $p = 0.13$). No statistically significant long-term trend in PDD is detectable over the 27-year Novo record.

The MPI ranged from 2 to 13 consecutive days with temperature above 0°C, with a period mean of 7.0 days (Supplementary Figure 1b). Melt onset ranged from DOY (Date Of Year) 1 to 18, indicating that the first occurrence of positive daily temperatures generally falls between 1 and 18 January. Freeze onset ranged from DOY 30 to 366, with a period mean of DOY 350 (Supplementary Figure 1c). The minimum freeze onset of DOY 30 (1999) reflects a year in which the brief melt season ended by 30 January, with no further positive temperatures recorded after that date; it does not imply an unusually late refreezing. Zero-curtain duration ranged from 7 to 21 days yr^{-1}, with a period mean of 14.4 days (Supplementary Figure 1d). OLS trend analysis yields no statistically significant trend in any of these metrics over the 1998–2025 period: MPI $p = 0.46$, melt onset $p = 0.50$, freeze onset $p = 0.09$, zero-curtain duration $p = 0.15$ (Supplementary Table 2).

The absence of statistically significant trends in the Novo atmospheric melt metrics over 1998–2025 does not contradict the ERA5-derived surface warming trend of +0.60 °C $decade^{-1}$ documented in section 5.3. ERA5 provides a gridded daily mean temperature record beginning in 1940 and captures the long-term multi-decadal warming signal across the 86-year period. The Novo AWS record covers only 27 years, limiting statistical power for trend detection. Additionally, the Novo station is located 53 km from the NIS centroid; sub-grid spatial heterogeneity, foehn-wind events, and localised radiative extremes at NIS may not be fully captured by the Novo daily mean record. The Novo metrics are therefore interpreted as characterising the regional atmospheric melt environment rather than as direct predictors of NIS surface melt.

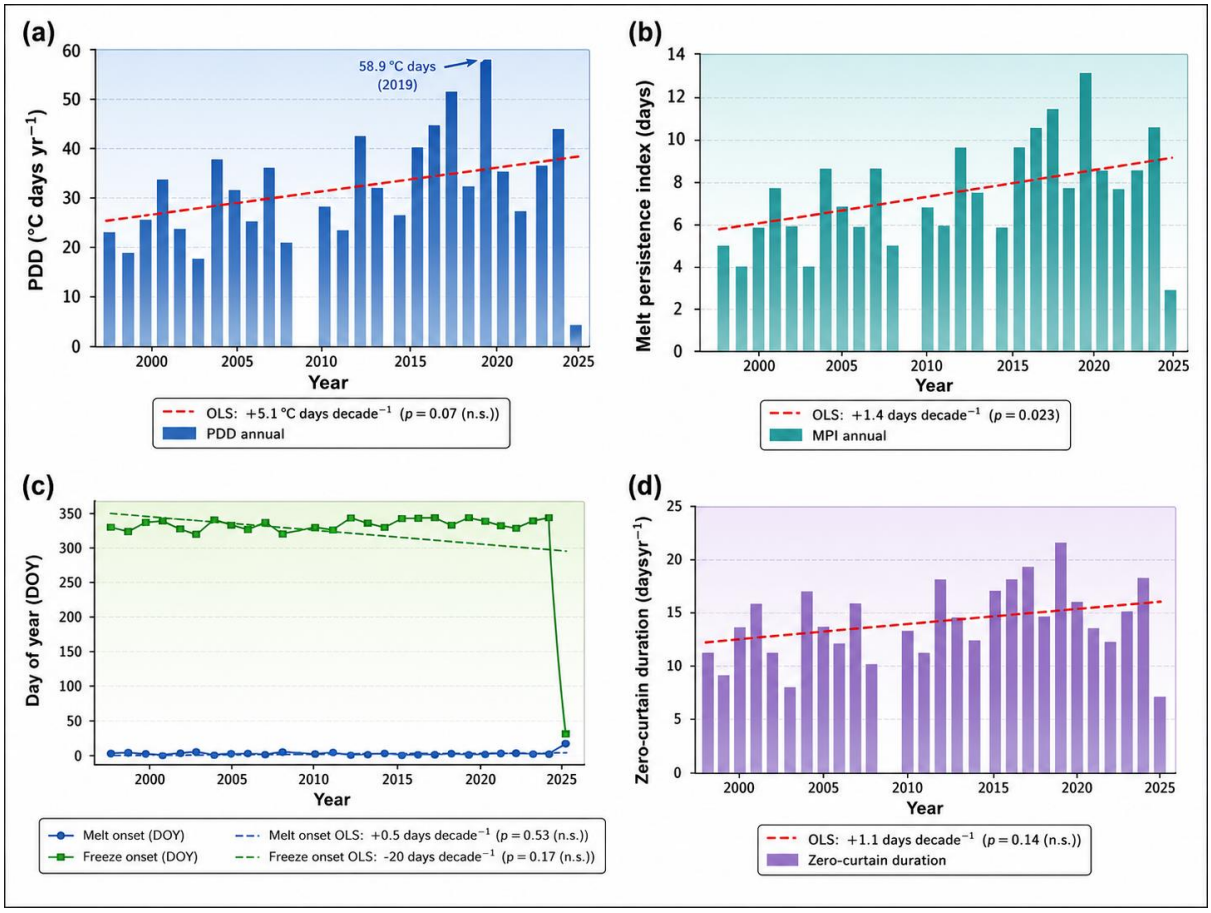

Supplementary Figure 1. Atmospheric melt metrics derived from Novo AWS daily temperature observations for 27 good-quality years, 1998–2025 (2009 excluded, insufficient data). Dashed lines show OLS regression trends. (a) Annual positive degree days. (b) Melt persistence index. (c) Melt onset (blue circles) and freeze onset (green squares). (d) Zero-curtain duration.

Supplementary Table 2. Atmospheric melt metrics derived from Novo AWS daily temperature observations. *Freeze onset DOY 30 (1999) reflects a year in which positive temperatures ended on 30 January; it does not indicate late-season refreezing.

Metric	Unit	Mean	Range (min – max)	OLS trend decade⁻¹	p-value	n
PDD	°C days yr⁻¹	28.5	4.0 – 58.9	+5.6 °C days	0.13	27
MPI	days	7.0	2 – 13	+0.6 days	0.46	27
Melt onset	DOY	4	1 – 18	+0.8 days	0.50	27
Freeze onset	DOY	350	30 – 366*	25.1 days	0.09	27
Zero-curtain duration	days yr⁻¹	14.4	7 – 21	+1.3 days	0.15	27

Supplementary Table 3. Comparison of thermal and geometric characteristics of selected Antarctic ice shelves. (NIS values correspond to the primary scenario (H = 312 m) and are compared with published estimates from other Antarctic ice shelves.

Ice Shelf	Location	H (m)	τ (yr)	T_s (°C)	acc	Pe[e]	T_{mid} (°C)	q^{base} (mW m^{-2})	M^b (mm yr^{-1})	Cavity	Reference
Nivlisen (NIS)[a]	cDML, E Antarctica	312	269	−17.6	0.52	4	−4.89	14.22	1.49	Cold-water	This study
Fimbulisen (S1)[b]	DML, E Antarctica	400	≈442	−15.0	0.10	1	≈−5 to −7[c]	n.r.	<600[d]	Cold/mixed	Humbert (2010)
Ross Ice Shelf	Ross Sea	200–600	≈120–870	−24 to −28	0.10–0.20	1–3	n.r.	n.r.	0–300	Cold-water	Gow (1963)
Roi Baudouin	cDML, E Antarctica	200–700	n.r.	−18 to −20	0.40–0.60	2–5	n.r.	n.r.	100–800	Cold, seasonal	Drews et al. (2017)
Amery	Prydz Bay, E Antarctica	≈400–1500	n.r.	−20 to −25	0.10–0.30	2–6	n.r.	n.r.	300–600	Cold-water	Wen et al. (2010)
Brunt/Stancomb-Wills	Weddell coast	100–400	n.r.	−20 to −24	0.20–0.40	1–3	n.r.	n.r.	100–500	Cold-water	Holland et al. (2015)

Note: [a] Primary scenario H = 312 m (Table 1). [b] S1 site; Jutulstraumen cold-core present. [c] Approximate from Humbert, (2010) [d] Excluding Jutulstraumen inflow zone. [e] Pe and τ for literature ice shelves estimated from published thickness and accumulation rates using Eqs. 3 and 9; not independently verified against borehole data for those shelves.

S4 Uncertainty assessment

This section provides a systematic assessment of the principal sources of uncertainty affecting the thermal model results presented in Sect. 5. The uncertainty characterisation follows the framework of Refsgaard et al., (2007), which distinguishes uncertainties arising from model structure, input data, boundary conditions, parameterisation, and numerical implementation. Because no borehole temperature observations currently exist for NIS, uncertainty characterisation rather than direct model validation is possible. The Fimbulisen S1 analogue comparison therefore provides a conservative upper bound on model-class structural uncertainty rather than an estimate of actual NIS model error.

S4.1 Model-class uncertainty characterisation

In the absence of in-situ borehole temperature observations at NIS, model-class structural uncertainty was characterised using the Fimbulisen S1 borehole temperature profile as a regional analogue, following the framework of Refsgaard et al., (2007). The same Robin, (1955) steady-state formulation was applied to Fimbulisen using representative parameters: $H = 400$ m, $T_s = -15.0$°C, $T_b = -2.0$°C, acc = 0.10 m i.e. yr^{-1}, $Pe = 1$. The modelled and observed Fimbulisen profiles are compared in Supplementary Figure 2a. The borehole observations were originally reported by Orheim et al, (1990) and digitised from Humbert, (2010).

The bias profile $B(z) = T_{model(z)} - T_{obs(z)}$ is shown in Supplementary Figure 2b. The model overestimates temperature (warm bias) throughout most of the column. The bias increases with depth from 2.36 °C at 10 m to a maximum of 17.38 °C at $z = 250$ m, before decreasing to near-zero at the base ($z = 395$ m, $B = -0.08$ °C). The column-mean bias is 12.58°C (depth-weighted, mean excluding BC points z=0, z=395). The boundary conditions at surface and base are satisfied by construction.

The large mid-column bias is attributed to the Jutulstraumen ice stream, which delivers cold ice from the interior of Dronning Maud Land into the Fimbulisen system. This cold-core advection produces an anomalously cold mid-column temperature profile that cannot be represented within a one-dimensional vertical conduction model (Humbert, 2010). No comparable cold-core advection mechanism has been reported for NIS. The Fimbulisen S1 borehole therefore represents a conservative, worst-case analogue for model-class structural uncertainty because it contains a strong cold-core advection signal that cannot be reproduced by a one-dimensional vertical model.

The NIS uncertainty envelope $U_{NIS(z)}$ was estimated by mapping the Fimbul bias onto the NIS column using normalised depth (Supplementary Figure 2c). The maximum U_{NIS} is ±8.69 °C, occurring at normalised depth $z/H \approx 0.63$ (~197 m in the primary NIS scenario). Because the Jutulstraumen cold-core advection responsible for the Fimbul bias has not been reported at NIS, the actual model-class uncertainty is expected to be substantially smaller than this conservative bound.

This uncertainty characterisation is not equivalent to direct model validation. The conservative nature of the Fimbul-derived uncertainty envelope means that the principal findings of near-surface warming, cold-content depletion, energy-barrier reduction, and the existence of a shallow warming layer overlying a deeper cooling layer remain qualitatively robust to plausible model-class structural uncertainty.

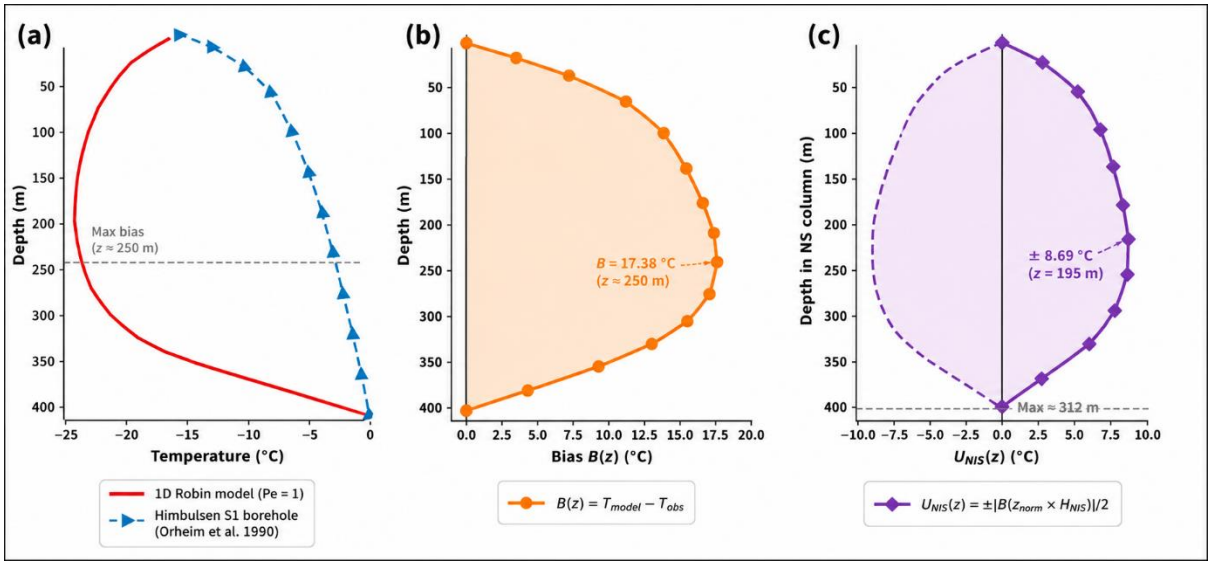

Supplementary Figure 2. Model-class uncertainty characterisation for the NIS 1D heat conduction model using the Fimbulisen S1 borehole as a regional analogue. (a) Comparison of the 1D Robin, (1955) model profile and Fimbulisen S1 borehole observations over the 0–395 m depth range. (b) Bias profile. (c) Conservative NIS uncertainty envelope.

S4.1.1 Model-class structural uncertainty

The dominant source of uncertainty arises from the structural limitations of the one-dimensional Robin, (1955) formulation. Comparison with the Fimbulisen S1 borehole profile was used to characterise this uncertainty, yielding a maximum envelope at z/H ≈ 0.63 (~197 m depth), giving $U_{NIS,max}$ = ±8.69 °C. This envelope is intentionally conservative because the dominant source of mismatch at Fimbulisen is cold-core advection associated with Jutulstraumen, a process that has not been reported at NIS. Consequently, the Fimbul-derived uncertainty envelope should be interpreted as a conservative upper bound rather than a realistic estimate of actual NIS model uncertainty.

S4.2 Ice-thickness uncertainty

The primary-scenario thickness (H=312 m) is derived from BedMachine Antarctica v4 (Morlighem et al., 2020),), with a representative uncertainty of ±10 m, giving ΔH/H ≈ 3.2%. For the thermal equilibration timescale, error propagation through Eq. 9 applies the relation:

$$\frac{\Delta\tau}{\tau} = 2\frac{\Delta H}{H} \qquad \text{(S1)}$$

This yields Δτ ≈ 17 yr. For the Péclet number (Eq. 2), the fractional thickness uncertainty propagates to ΔPe ≈ 0.13, and for basal conductive heat flux, Δq_{base} ≈ 0.46 mW m^{-2}. These uncertainties are approximately 3% of the primary-scenario values. The six-scenario ensemble explored in Sect. 5 spans a substantially larger thickness range than the

estimated BedMachine Antarctica v4 uncertainty and therefore provides a useful sensitivity envelope.

S4.3 Accumulation-rate uncertainty

The primary accumulation rate (acc=0.52 m i.e. yr^{-1}) is derived from Pratap et al., (2022). Sensitivity experiments spanning $0.37 \leq$ acc ≤ 0.64 m i.e. yr^{-1} produce Péclet numbers in the range Pe = 3.2–4.9, with $\Delta Pe \approx \pm 0.85$ and $\Delta T_m^{Id} \approx \pm 0.3$ °C. The primary-scenario interpretation of NIS as an intermediate conduction–advection system (Pe = 4) remains qualitatively unchanged across this range.

S4.4 ERA5 forcing uncertainty

The ERA5 Antarctic temperature uncertainty (ΔT_s) is commonly reported as approximately ±0.5°C relative to station observations (Gossart et al., 2019; Hersbach et al., 2020). The pre-satellite ERA5 back-extension carries larger uncertainty of ≈ ±1−2°C before 1979 (Poli et al., 2016). A systematic forcing bias primarily shifts absolute temperatures throughout the vertical profile but has limited influence on trend slopes, sign-reversal depth, percentage cold-content changes, and percentage energy-barrier changes. Consequently, ERA5 forcing uncertainty affects absolute temperatures more strongly than the principal transient metrics employed in this study.

S4.5 Basal boundary condition

Basal temperature is prescribed as the seawater freezing point ($T_b = -1.90$ °C). For a salinity uncertainty of ±0.5 psu, the propagated basal temperature uncertainty is $\Delta T_b \approx \pm 0.004$ °C, which is negligible relative to all other uncertainty sources.

S4.6 Firn-density parameterisation

The prescribed density profile is based on literature-derived firn densification behaviour and is applied consistently throughout the transient simulation to calculate cold-content and seasonal-wave metrics. Alternative density profiles were not explicitly evaluated, as no site-specific firn-core observations currently exist for NIS. This uncertainty primarily affects cold content (CC and CC_{col}), the energy barrier ($E_{barrier}$), seasonal penetration depth, and thermal-wave damping. Although the absolute values of these quantities may vary under alternative density profiles, the temporal trends and relative percentage changes reported here are expected to be substantially less sensitive, since the same density formulation is applied consistently throughout the simulation.

S4.7 One-dimensional model assumption

The model assumes horizontal homogeneity and excludes lateral heat transport, grounding-line thermodynamics, outlet-glacier cold-core advection, and spatially variable ocean forcing. This introduces an unquantified structural uncertainty. However, unlike Fimbulisen, NIS has no reported major cold-core outlet glacier, making the one-dimensional approximation appropriate for characterising shelf-mean thermal conditions.

S4.8 Numerical discretisation

Numerical convergence testing confirmed truncation error of order $O(\Delta z^2, \Delta t)$ with a residual below 10^{-6} °C. Numerical uncertainty is therefore negligible (< 0.001 °C) relative to all physical uncertainty sources considered in this study.

S4.9 Combined parameter uncertainty

The principal quantified parameter uncertainties are ice-thickness uncertainty U_H = 3.2%, accumulation-rate uncertainty U_{acc} = 5.0%, and ERA5 forcing uncertainty U_{ERA5} = 5.0%. Combining these in quadrature using root-sum-square propagation:

$$U_{param}=\sqrt{U_H^2 + U_{acc}^2 + U_{ERA5}^2} \quad \text{(S2)}$$

Evaluating with the values above gives 7.8%, yielding a combined quantified parameter uncertainty of approximately ±8% on the primary thermal-regime metrics. By comparison, the Fimbulisen-derived structural envelope (±8.69 °C) corresponds to approximately 55% of the total NIS thermal range and therefore remains substantially larger than the propagated parameter uncertainty. This value should not be interpreted as an uncertainty on individual outputs but rather as a conservative upper bound on model-class structural uncertainty.

Overall, while absolute temperatures at depth remain subject to structural uncertainty in the absence of borehole observations, the principal findings of this study, including near-surface warming, deep-column cooling, the ~27 m sign-reversal depth, cold-content depletion, $E_{barrier}$ reduction, and the interpretation of progressive thermal preconditioning, remain qualitatively unchanged across the quantified uncertainty range. The uncertainty inventory is summarised in Supplementary Table 4.

Supplementary Table 4. Summary of principal uncertainty sources for the NIS 1D heat conduction model. Subsection numbers (S4.1 – S4.7) correspond to discussion in Sect. S4. U_{NIS} = NIS uncertainty envelope (Sect. S4.1). n.q. = not quantified. FD = finite difference. SMB = surface mass balance. BC = boundary condition.

Uncertainty source	Basis / estimate	Estimated magnitude	Affected outputs	Notes
S4.1 Model-class structural	Fimbul S1 analogue	$U_{NIS,max}$ = ±8.69 °C at z/H ≈ 0.63 (~197 m)	T(z), T_{mid}, q_{base}, Mb	Conservative upper bound. Dominant Fimbul bias arises from Jutulstraumen cold-core advection, which has not been reported at NIS; therefore the envelope is interpreted as a conservative bound rather than an estimate of actual NIS uncertainty.
S4.2 Ice thickness H	BedMachine Antarctica v4	τ ±17 yr; Pe ±0.1; q_{base}	Pe, τ, q_{base}, Mb	Approximately 3 % of primary-scenario values. The six-scenario

	(±10 m, ~3 %)	±0.46 mW m^{-2}		ensemble spans a thickness range substantially larger than the estimated BedMachine Antarctica v4 uncertainty and therefore provides a useful sensitivity envelope.
S4.3 Accumulation rate	SMB range 0.37–0.64 m i.e. yr^{-1}	Pe = 3.2–4.9 (primary Pe = 4); T_{mid} ±0.3 °C	Pe, T_{mid}, τ (minor)	Primary scenario (acc = 0.52 m i.e. yr^{-1}) represents the best-estimate SMB.
S4.4 ERA5 surface forcing + pre-1979 back-extension	ERA5 errors commonly of order ±0.5 °C relative to Antarctic station observations; pre-1979 uncertainty ±1–2 °C	~±0.5 °C shift in absolute T(z); larger uncertainty in early transient period	T(z), CC, CC_{col}, $E_{barrier}$ (absolute values)	Primarily affects absolute temperatures. Relative changes, percentage reductions, and long-term trends are substantially less sensitive to a uniform forcing bias.
S4.5 Basal boundary condition (T_b)	Salinity ±0.5 psu → $\Delta T_b \approx$ ±0.004 °C	Negligible	T_b only	Pressure-melting point is well constrained.
S4.6 Firn-density parameterisation	Prescribed density profile derived from literature-based firn densification behaviour	n.q.	CC, CC_{col}, $E_{barrier}$, seasonal-wave metrics	Alternative density profiles were not explicitly evaluated. Represents an unquantified source of uncertainty affecting thermal-storage calculations.
S4.7 1D model structure	Horizontal homogeneity assumption; no lateral advection	n.q.	T(z) in complex-flow regions	NIS lacks a reported cold-core outlet glacier; 1D formulation considered appropriate for shelf-mean conditions.
S4.8 Numerical discretisation	FD multi-zone grid; ε = 10^{-6} °C	Negligible (<0.001 °C)	All outputs	Grid-convergence confirmed; truncation error $O(\Delta z^2, \Delta t)$.
S4.9 Combined parameter uncertainty	RSS combination of thickness, accumulation	±8%	All primary thermal metrics	Quantified parameter uncertainty. Smaller than the Fimbulisen-derived structural envelope (±8.69°C; ~55% of total NIS

	and ERA5-forcing uncertainties			thermal range), which is treated as a model-structural upper bound.

S5 Limitations and model assumptions

S5.1 Temporal consistency of datasets

This study combines ERA5 atmospheric forcing (1940–2025), present-day BedMachine Antarctica v4 geometry, and multi-decadal accumulation-rate estimates. Consequently, the simulations quantify the response of the present-day NIS configuration to historical atmospheric forcing and do not reconstruct temporal changes in ice thickness, accumulation rate, or ocean boundary conditions. Ice thickness and accumulation rate are therefore treated as time-invariant parameters throughout the simulations.

Ocean boundary conditions are similarly held constant at the seawater freezing point (T_b=−1.90°C). Satellite-derived basal melt rates for NIS (~800 mm yr^{-1}; Rignot et al., 2013) greatly exceed the conductive melt component estimated here (1.49 mm yr^{-1}), indicating that ocean-driven basal melting dominates the basal mass balance. The present model therefore characterises the conductive thermal regime and near-surface thermal evolution rather than the total basal melt budget.

S5.2 One-dimensional model framework

The model assumes one-dimensional vertical heat transfer and neglects lateral heat transport, grounding-line thermodynamics, spatially variable ocean forcing, and outlet-glacier cold-core advection. These simplifications are appropriate for characterising the shelf-mean thermal regime but may not capture local thermal heterogeneity. Firn densification is prescribed rather than dynamically modelled and therefore does not represent interannual variability in firn properties. The omission of explicit advection in the transient formulation is justified because the objective is to quantify the propagation of atmospheric temperature anomalies through a background thermal structure already established using the Robin, (1955) advection–conduction solution.

S5.3 Absence of direct borehole observations

No borehole temperature measurements currently exist for NIS. Consequently, absolute temperatures, englacial thermal structure, and the presence of any temperate basal layers cannot be directly validated. The Fimbulisen analogue comparison provides a conservative estimate of model-class uncertainty but cannot replace site-specific observations. Borehole thermistor measurements remain the highest-priority requirement for future validation of the thermal profile presented here.

S5.4 ERA5 forcing limitations

The ERA5 provides spatially averaged atmospheric conditions at approximately 0.25° resolution and does not resolve local-scale temperature anomalies, short-duration melt events, or the full surface energy balance. In addition, uncertainty is larger prior to the satellite era.

These limitations primarily affect absolute temperatures and local melt representation but do not alter the long-term warming trends identified in this study.

S5.5 Transient-model simplification

The transient simulations neglect explicit vertical advection and represent the propagation of atmospheric temperature anomalies through an advection-influenced background thermal state established using the Robin, (1955) steady-state solution. Consequently, the transient results should be interpreted as first-order estimates of long-term thermal adjustment rather than a complete thermodynamic reconstruction of NIS evolution.

S5.6 Future directions

Future work should prioritise (i) borehole thermistor installations, (ii) firn-core density and temperature measurements, (iii) ocean-cavity observations, (iv) repeat ApRES surveys, (v) on-shelf surface energy-balance monitoring, and (vi) coupled two- and three-dimensional ice–ocean thermal modelling. These observations would provide the data required to directly validate and refine the first thermal baseline presented here.

S5. Illustrative Linear thermal projections to 2075

S5.1 Rationale and scope

The statistically significant OLS trends documented in Sect. 5.3 (surface warming), Sect. 5.4 (cold-content depletion), and Sect. 5.6 (energy-barrier reduction) provide a basis for illustrative linear extrapolation beyond the 2025 observational endpoint. Such projections are presented here for four parameters: the annual maximum ERA5 surface skin temperature (T_{max}), the temperature at 100 m depth (T_{100}), the volumetric cold content at 1 m depth (CC), and the energy barrier to surface melt ($E_{barrier}$) (Hersbach et al., 2020). These are the four metrics most directly linked to the thermal preconditioning and melt-susceptibility framework developed in Sects. 5.3–5.6.

Important caveat. All projections in this section are linear extrapolations of observed OLS trend slopes, not outputs from a climate model, a physically coupled ice–ocean model, or a scenario-based forcing experiment. They assume that the observed linear trends in ERA5 surface temperature and model-derived subsurface temperatures continue unchanged to 2075, an assumption that does not account for non-linear climate feedbacks, changes in atmospheric circulation, ice-shelf dynamic responses, or ocean forcing variability. The projections are therefore presented as illustrative quantitative benchmarks that characterise the trajectory of thermal preconditioning under observed forcing rates, consistent with the framing of Sect. 5.6 (melt-threshold linear extrapolation). They should not be interpreted as predictions.

S5.2 Projection methodology

S5.2.1 OLS trend line construction

For each parameter, the OLS regression line is defined by its slope S (in units per year) and an intercept derived from the mean-year anchor. Because the OLS slope minimises the sum of squared residuals across all 86 annual observations rather than connecting the 1940 and 2025 endpoints exactly, the regression line does not generally pass through the observed endpoint values. The OLS line is constructed as:

$$\theta(y) = \bar{\theta} + S\,(y - \bar{y}) \quad \text{(S3)}$$

where θ(y) is the OLS line value at year y, $\bar{\theta}$ is the parameter mean over 1940–2025, S is the OLS slope (units per year), and $\bar{y} = 1982.5$ is the mean year of the 86-year record. The parameter mean is estimated as $\bar{\theta} \approx (\theta_{1940} + \theta_{2025}) / 2$, using the observed 1940 and 2025 values from the manuscript. The resulting OLS intercept is:

$$b = \bar{\theta} - S\,\bar{y} \quad \text{(S4)}$$

For projection beyond 2025, the extrapolated value at year y > 2025 is:

$$\theta(y) = b + S \cdot y = \theta(2025) + S\,(y - 2025) \quad \text{(S5)}$$

where θ (2025) is the OLS line value at 2025 (not the observed 2025 endpoint). This distinction is small but scientifically important: the OLS line at 2025 is the regression estimate, which may differ from the actual observed value at 2025 because the OLS line

represents the best linear fit to all 86 data points, not an interpolation through the endpoints. The OLS line values at 2025 and 2075 are reported in Supplementary Table 5; observed 2025 endpoint values are also listed for completeness.

S5.2.2 Confidence interval propagation

The 95 % confidence interval on each projected value is derived from the OLS slope uncertainty (Table 4). The CI on the slope, σS (in °C decade^{-1} or equivalent), widens the projection envelope linearly with time beyond 2025. For a projection τ = y − 2025 years into the future, the 95 % CI on the projected value is:

$$CI_{95}(y) = \theta(y) \pm \frac{\sigma S \cdot \tau}{10} \quad \text{(S6)}$$

where σS is the 95 % CI half-width on the slope in units per decade (from Table 4), and τ / 10 converts the 50-year projection horizon to decades. This formulation assumes that the slope uncertainty is the dominant source of projection uncertainty, a valid assumption given that the OLS intercept uncertainty is small relative to the slope uncertainty at the decadal timescale. The CI envelopes for each parameter are summarised in Supplementary Table 5 and shown in Supplementary Figure 4.

Note that for T_{100}, the near-perfect OLS fit (R^2 = 0.995, 95 % CI = ±0.004°C decade^{-1}) produces an extremely narrow CI envelope (±0.02°C at 2075), consistent with the monotonic and systematic nature of the deep-column cooling signal (Sect. 5.3). In contrast, the T_{max} projection carries a substantially wider CI (±0.40°C at 2075), reflecting the high interannual variability of the annual maximum temperature relative to its long-term trend.

S5.2.3 Axis assignment and figure construction

All four parameters share a common x-axis (year, 1940–2075) in Supplementary Figure 4. Two y-axes are employed to accommodate the different physical units of the four parameters:

Left y-axis (temperature, °C): annual maximum surface skin temperature T_{max} and temperature at 100 m depth T_{100}. Both parameters are plotted on the same temperature scale, with T_{max} in the range −3 to 0°C and T_{100} in the range −12 to −7°C, separated on the axis by their physical magnitude.

Right y-axis (thermal energy): volumetric cold content CC (MJ m^{-2}) and energy barrier $E_{barrier}$ (MJ m^{-3}). Despite the nominally different SI units (m^{-2} vs m^{-3}), both parameters are numerically evaluated at a single reference depth (1 m) and share a similar magnitude range (~20–41), making a shared energy axis appropriate for the purposes of this comparison figure.

Solid lines show the OLS trend line over the observed record (1940–2025); dashed lines show the linear extrapolation to 2075. The 95 % CI envelope widens from the 2025 anchor. Two reference lines are included on the left axis: the 0°C melt threshold and the steady-state Robin temperature at 100 m ($T_{100, ss}$ = −7.25°C), which serves as the long-term equilibrium reference for the deep-column cooling trajectory.

S5.3 Projected values and interpretation

Projected values for all four parameters at 2075 under continued linear OLS trends are summarised in Supplementary Table 5 and illustrated in Supplementary Figure 4. Each parameter is discussed below.

S5.3.1 Annual maximum surface temperature (T_{max})

The OLS trend of +0.12°C decade^{-1} projects the ERA5 annual maximum skin temperature from −1.24°C (OLS line at 2025) to −0.64°C at 2075 (±0.40°C; 95 % CI). The OLS line does not cross the 0°C melt threshold within the 2075 projection horizon; under strictly continued linear forcing, the 0°C crossing occurs at approximately 2128. This does not imply the absence of surface melt within the 2025–2075 window: the T_{max} signal represents an ERA5 grid-cell daily mean, and sub-grid and sub-daily mechanisms (foehn advection, radiative heating, melt–albedo feedback) already produce documented surface melt at NIS despite sub-freezing ERA5 daily means. The projection demonstrates that the ERA5-scale thermal resistance to melt is declining at a statistically robust rate and will reduce further over the coming decades.

S5.3.2 Temperature at 100 m depth (T_{100})

The deep-column cooling trend of −0.23°C decade^{-1} (R^2 = 0.995) projects T_{100} from −9.15°C (OLS line at 2025) to −10.30°C at 2075 (±0.02°C; 95 % CI). This continued monotonic cooling of the deep column is the projected manifestation of the non-equilibrium thermal adjustment documented in Sect. 6.3. The deep column is moving progressively further from its steady-state reference (T_{100}, ss = −7.25°C), consistent with the thermal equilibration timescale τ = 269 yr substantially exceeding the observational record. Under the linear projection, the total deepening of T_{100} below the 1940 baseline will reach approximately 3.0°C by 2075. This deep cooling does not contribute to near-surface melt susceptibility but represents a scientifically significant non-equilibrium signature of centennial-scale thermal inertia in the NIS ice column.

S5.3.3 Cold content at 1 m depth (CC)

The OLS depletion rate of −1.04 MJ m^{-2} decade^{-1} projects CC at 1 m from 27.51 MJ m^{-2} (OLS line at 2025) to 22.31 MJ m^{-2} at 2075 (±2.60 MJ m^{-2}; 95 % CI). Relative to the 1940 baseline of 38.96 MJ m^{-2}, this represents a total depletion of 42.7 % by 2075. The near-surface cold reservoir at 1 m depth governs the refreezing capacity of the firn column: each MJ m^{-2} of cold content lost represents a reduction in the thermal energy available to refreeze percolating meltwater. A 42.7 % reduction from the 1940 baseline implies that by 2075, the near-surface firn will have less than three-fifths of its original refreezing capacity, substantially increasing the likelihood of meltwater persistence and supraglacial ponding under the melt-favourable atmospheric conditions documented in Sect. 6.4–6.5.

S5.3.4 Energy barrier to surface melt ($E_{barrier}$)

The OLS depletion rate of −1.09 MJ m^{-3} decade^{-1} projects $E_{barrier}$ from 27.75 MJ m^{-3} (OLS line at 2025) to 22.30 MJ m^{-3} at 2075 (±2.73 MJ m^{-3}; 95 % CI). Relative to the 1940 baseline of 40.05 MJ m^{-3}, this represents a total reduction of 44.3 % by 2075. $E_{barrier}$ quantifies the volumetric energy input required to warm 1 m^3 of surface ice from the annual

mean temperature to 0°C; a sustained reduction in this quantity means that progressively less atmospheric energy is required to initiate surface melting. The projected continued decline is physically consistent with the ongoing ERA5 surface warming trend and provides an energy-based quantification of the progressive reduction in thermal resistance to melt initiation at NIS over the coming decades.

S5.3.5 Convergence of near-surface metrics

The near-identical projected depletion rates of CC (42.7 %) and $E_{barrier}$ (44.3 %) by 2075 reflect their shared physical basis: both metrics are proportional to (0 − T) through the same ρcp factor and are driven by the same ERA5 surface warming trend. Their convergence in projected values (~22 MJ m⁻ by 2075) reinforces the internal consistency of the thermal preconditioning framework and confirms that the near-surface depletion signal is robust to the choice of metric. The combined picture from T_{max}, CC, and $E_{barrier}$ projections is unambiguous: under continuation of observed trends, NIS will by 2075 have substantially lower thermal resistance to surface melt than it does today, with the ERA5-scale annual maximum temperature approaching the 0°C threshold within the following half-century.

Supplementary Table 5. Summary of linear projection values for four NIS thermal parameters under continuation of observed OLS trends to 2075. OLS line values at 2025 and 2075 are derived from the mean-year anchored regression line (Eqs. S3-S5); observed 2025 endpoint values are listed separately for comparison. 95 % CI at 2075 propagated from Table 4 slope uncertainties (Eq. S6).

Parameter	1940 observed	2025 observed	2075 projected (OLS line)	Notes
Annual max surface temp, T_{max} (°C); OLS +0.12°C decade^{-1}	−2.89°C	−0.61°C (obs.) −1.24°C (OLS line)	−0.64°C ± 0.40°C	Left axis. OLS line crosses 0°C at ~2128 under continued linear trend.
Temp. at 100 m depth, T_{100} (°C); OLS −0.23°C decade^{-1}, R^2=0.995	−7.26°C	−9.09°C (obs.) −9.15°C (OLS line)	−10.30°C ± 0.02°C	Left axis. Near-perfect R^2 constrains CI tightly. Deep cooling is non-equilibrium adjustment (τ=269 yr). Steady-state reference: −7.25°C.
Cold content at 1 m, CC (MJ m^{-2}); OLS −1.04 MJ m^{-2} decade^{-1}	38.96 MJ m^{-2}	24.91 MJ m^{-2} (obs.) 27.51 MJ m^{-2} (OLS line)	22.31 MJ m^{-2} ± 2.60	Right axis. 42.7% total depletion from 1940 baseline by 2075 (OLS line).
Energy barrier, $E_{barrier}$ (MJ m^{-3}); OLS −1.09 MJ m^{-3}	40.05 MJ m^{-3}	24.72 MJ m^{-3} (obs.) 27.75 MJ m^{-3} (OLS line)	22.30 MJ m^{-3} ± 2.73	Right axis. 44.3% total depletion from 1940 baseline by 2075 (OLS line).

decade^{-1}				

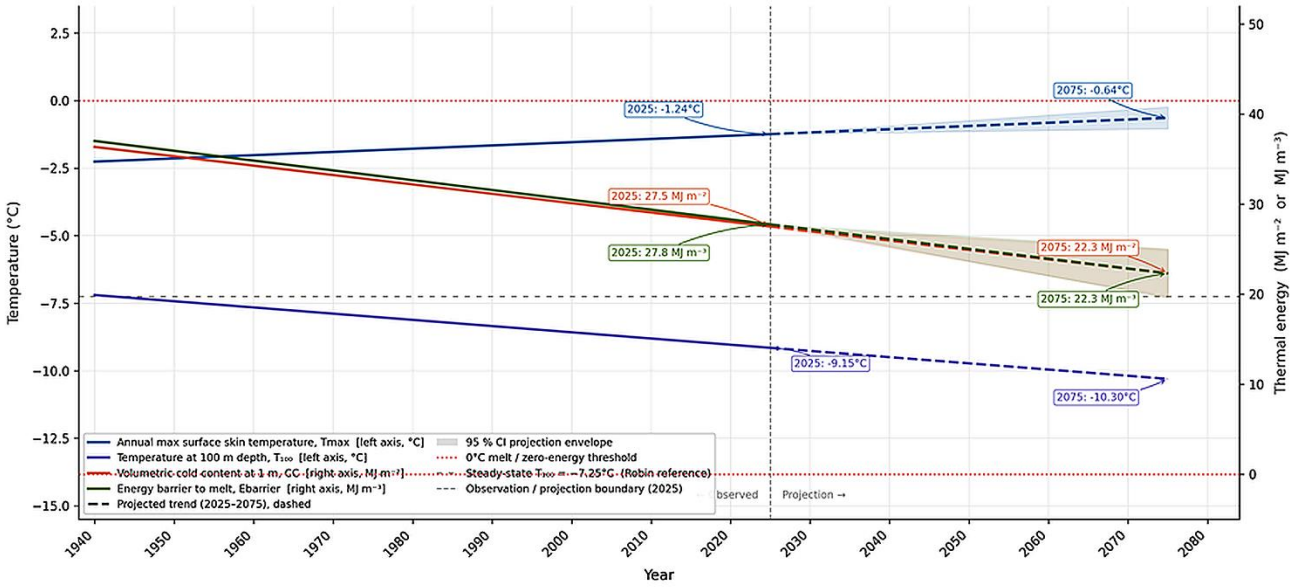

Supplementary Figure 4. Thermal-regime projections for Nivlisen Ice Shelf (primary scenario, H = 312 m) to 2075 under continuation of observed OLS trends (1940–2025). Four parameters are plotted on a shared x-axis (year) against two y-axes: temperature in °C (left) and thermal energy in MJ m^{-2} or MJ m^{-3} (right).

S5.4 Limitations of linear extrapolation

The linear extrapolations presented in Sect. S5.3 and Supplementary Figure 4 are subject to the following specific limitations, in addition to the general caveat stated in Sect. S5.1.

(i) Stationarity assumption. The projection assumes that the ERA5 surface warming trend of +0.60°C decade^{-1} continues at its observed rate. Observed global warming trends are not stationary: accelerated warming under higher emission scenarios, or a slowdown under mitigation, would respectively steepen or shallow the projected trajectories. The projection therefore represents a single scenario defined by historical trend continuation, not an ensemble or probabilistic forecast.

(ii) Non-linear firn and ice responses. At sufficiently low cold-content values, the firn column may undergo non-linear transitions: saturation of pore space, formation of ice lenses, or complete absence of a refreezing buffer. These thresholds are not represented in the linear projection. The actual depletion rate of CC may accelerate as the cold reservoir diminishes, making the linear projection a conservative lower bound on depletion rate at low CC values.

(iii) Deep-column projection validity. The T_{100} projection is the most physically robust of the four, given the near-perfect $R^2 = 0.995$ of the observed trend and its mechanistic explanation (non-equilibrium adjustment toward colder equilibrium at $\tau = 269$ yr). However, the linear trend in T_{100} is itself a manifestation of the non-linear approach toward thermal equilibrium (exponential in time for a step forcing). The linear approximation is valid for short projection horizons ($\tau / \tau \ll 1$) but will eventually overestimate the rate of deep-column cooling as the column approaches equilibrium on centennial timescales.

(iv) Static model geometry. The NIS thermal model uses present-day BedMachine v4 geometry throughout ((Morlighem et al., 2020). Continued ice-shelf thinning — documented in cDML by Rignota et al., 2019), would reduce H and hence τ, potentially accelerating the near-surface thermal response relative to the projection. This effect is not captured in the linear extrapolation.

References

A. Gossart AND S. Helsen,J. T. M. Lenaerts,S. Vanden Broucke,N. P.M. Van Lipzig, A. N. S. (2019). An evaluation of surface climatology in state-of-the-art reanalyses over the Antarctic Ice Sheet. *Journal of Climate*, *32*(20), 6899–6915. https://doi.org/10.1175/JCLI-D-19-0030.1

E. Rignot, S. Jacobs, J. Mouginot, B. S. (2013). Ice-Shelf Melting Around Antarctica. *Science*, *341*(6143), 266–270. https://doi.org/10.1126/science.1235798

Eric Rignota, J ´er ´emie Mouginot, Bernd Scheuchl, Michiel van den Broeke, Melchior J. van Wessem, and M. M. (2019). Four decades of Antarctic ice sheet mass balance from 1979–2017. *Proceedings of the National Academy of Sciences of the United States of America*, *116*(4), 1095–1103. https://doi.org/10.1073/pnas.1812883116

Hersbach, H., Bell, B., Berrisford, P., Hirahara, S., Horányi, A., Nicolas, J., Peubey, C., Radu, R., Bonavita, M., Dee, D., Dragani, R., Flemming, J., Forbes, R., Geer, A., Hogan, R. J., Janisková, H. M., Keeley, S., Laloyaux, P., Cristina, P. L., & Thépaut, J. (2020). The ERA5 global reanalysis. *Quarterly Journal Ofthe Royal Meteorological Society*, *146*(730), 1999–2049. https://doi.org/10.1002/qj.3803

Humbert, A. (2010). The temperature regime of Fimbulisen, Antarctica. *Annals of Glaciology*, *51*(55), 56–64. https://doi.org/10.3189/172756410791392673

Jens Christian Refsgaard , Jeroen P. van der Sluijs, Anker Lajer Højberg, P. A. V. (2007). Uncertainty in the environmental modelling process A framework and guidance. *Environmental Modelling & Software*, *22*(11), 1543–1556. https://doi.org/10.1016/j.envsoft.2007.02.004

Lindbäck, K., Moholdt, G., Nicholls, K. W., Hattermann, T., Pratap, B., Thamban, M., & Matsuoka, K. (2019). Spatial and temporal variations in basal melting at Nivlisen ice shelf, East Antarctica, derived from phase-sensitive radars. *Cryosphere*, *13*(10), 2579–2595. https://doi.org/10.5194/tc-13-2579-2019

Mathieu Morlighem, Eric Rignot, Tobias Binder, Donald Blankenship, Reinhard DREWS, Graeme Eagles, Olaf Eisen, Fausto Ferraccioli, Ren´e Forsberg, Pe- ter Fretwell, Vikram Goel, Jamin S. Greenbaum, Hilmar Gudmundsson, Jingxue Guo, Veit Helm, Coen HOFSTED, D. Y. (2020). Deep glacial troughs and stabilizing ridges unveiled be- neath the margins of the Antarctic ice sheet. *Nature Geoscience*, *13*, 132–137. https://doi.org/10.1038/s41561-019-0510-8

Murugesan, G. P., Koppuram Ramesh Babu, R., Baineni, M., Chidananda, R., Satish, D., Sivalingam, S., Aruldhas, D. J., Venkatesh, K., Muniswamy, N. K., & Luis, A. J. (2023). Decoding the Dynamics of Climate Change Impact: Temporal Patterns of Surface Warming and Melting on the Nivlisen Ice Shelf, Dronning Maud Land, East Antarctica. *MDPI Remote Sensing*, *15*(24), 1–21. https://doi.org/10.3390/rs15245676

Orheim, O., Hagen, J.O., Österhus, S. and Sætrang, A. C. (1990). Studies on, and underneath, the ice shelf Fimbulisen. *Nor. Polarinst. Medd.*, *113*, 59–73. https://hdl.handle.net/11250/4631965

Padman, L., Fricker, H. A., Coleman, R., Howard, S., & Erofeeva, L. (2002). A new tide model for the Antarctic ice shelves and seas. *Annals of Glaciology*, *34*, 247–254. https://doi.org/10.3189/172756402781817752

Poli, P., Hersbach, H., Dee, D. P., Berrisford, P., Simmons, A. J., Vitart, F., Laloyaux, P., Tan, D. G. H., Peubey, C., Thépaut, J.-N., Trémolet, Y., Hólm, E. V., Bonavita, M., Isaksen, L., & Fisher,

and M. (2016). ERA-20C : An Atmospheric Reanalysis of the Twentieth Century. *American Meteorological Society*, *29*, 4083–4097. https://doi.org/10.1175/JCLI-D-15-0556.1

Pratap, Bhanu, Rahul Dey , Kenichi Matsuoka, G. M., & Lindbäck, Katrin, Vikram Goel, C. M. L. and M. T. (2022). Three-decade spatial patterns in surface mass balance of the Nivlisen Ice Shelf, central Dronning Maud Land, East Antarctica. *Journal of Glaciology*, *68*(267), 174–186. https://doi.org/10.1017/jog.2021.93

Robin, G. de Q. (1955). Ice Movement and Temperature Distribution in Glaciers and Ice Sheets. *Cambridge University Press*, *2*(18), 523–532. https://doi.org/10.3189/002214355793702028

Trusel, L. D., Frey, K. E., Das, S. B., Munneke, P. K., Trusel, L. D., Frey, K. E., Das, S. B., & Munneke, P. K. (2013). Satellite-based estimates of Antarctic surface meltwater fluxes Satellite-based estimates of Antarctic surface meltwater fl uxes. *Geophysical Research Letters*, *40*, 6148–6153. https://doi.org/10.1002/2013GL058138